WAVE INTERACTIONS WITH ARRAYS OF BOTTOM-MOUNTED CIRCULAR CYLINDERS:

INVESTIGATION OF OPTICAL AND ACOUSTICAL ANALOGIES

A Thesis

by

ALDRIC BAQUET

Submitted to the Office of Graduate Studies of
Texas A&M University
in partial fulfillment of the requirements for the degree of

MASTER OF SCIENCE

August 2010

Major Subject: Ocean Engineering

WAVE INTERACTIONS WITH ARRAYS OF BOTTOM-MOUNTED CIRCULAR CYLINDERS:

INVESTIGATION OF OPTICAL AND ACOUSTICAL ANALOGIES

A Thesis

by

ALDRIC BAQUET

Submitted to the Office of Graduate Studies of
Texas A&M University
in partial fulfillment of the requirements for the degree of

MASTER OF SCIENCE

Approved by:

Chair of Committee,	Richard Mercier
Committee Members,	Jun Zhang
	Achim Stoessel
Head of Department,	John Niedzwecki

August 2010

Major Subject: Ocean Engineering

ABSTRACT

Wave Interactions with Arrays of Bottom-mounted Circular Cylinders: Investigation of Optical and Acoustical Analogies. (August 2010)

Aldric Baquet, B.S., Ecole Spéciale des Travaux Publics

Chair of Advisory Committee: Dr. Richard Mercier

Wave scattering by arrays of cylinders has received special attention by many authors and analytical solutions have been derived. The investigation of optical and acoustical analogies to the problem of interaction of water waves with rigid and flexible cylinder arrays is the main focus of this thesis. In acoustics, a sound may be attenuated while it propagates through a layer of bubbly liquid. In fact, if the natural frequency of the bubbles is in the range of the wave periods, the attenuation becomes more evident. The ultimate objective of the research described herein is to determine if this phenomenon may also be found in the interaction between water waves and arrays of flexible cylinders.

In a first approach, arrays of rigid cylinders are studied in shallow water. The array is treated as an effective medium, which allows for the definition of reflection and transmission coefficients for the array, and theories from Hu and Chan (2005) associated with the Fabry-Pérot interferometer are compared against direct computations of wave scattering using the commercial code WAMIT. Reflection and transmission coefficients from WAMIT are evaluated by applying a Maximum Likelihood Method. The results

from WAMIT were found to be in good agreement with those obtained from the effective medium theory. Due to observed inconsistencies for short wave periods and small incident angles, the effective width of the medium is defined and corrected.

For the case of a flexible cylinder, generalized modes corresponding to deformations of the cylinder's surface are formulated and added to WAMIT's subroutine. Equations of motion are derived from the theory of vibration for thin shells and mass and stiffness matrices are defined. The objective is to maximize wave attenuation from the array of flexible cylinders. Therefore, the natural periods of the "breathing" mode for these cylinders is set in the range of the studied wave periods. Then, material properties, as well as mass and stiffness matrices, are chosen to achieve this effect.

ACKNOWLEDGEMENTS

I would like to thank my committee chair, Dr. Mercier, and my committee members, Dr. Zhang and Dr. Stoessel, for their guidance and support throughout the course of this research.

Thanks also go to my friends and the department faculty and staff for making my time at Texas A&M University a great experience.

Finally, thanks to my family for their encouragement.

TABLE OF CONTENTS

Page

LIST OF FIGURES

FIGURE Page

FIGURE Page

LIST OF TABLES

1. INTRODUCTION

1.1 Motivation and objectives

Interactions of water waves with cylinder arrays, consisting of both floating or bottom-mounted cylinders, have received particular attention due to the wide range of application. By trapping and reflecting wave energy, arrays of cylinders can be used for coastal protection. For certain geometries, cylinder arrays can focus wave energy to a particular point in the wave field. This can be useful to improve the performance of a wave energy device.

Many previous studies have been done regarding scattering by individual cylinders and cylinder arrays. The scope of this thesis is to investigate analogous theories from optics and acoustics to study interactions between waves and cylinder arrays.

Hu and Chan (2005) have investigated analogies with optics. Defining the array of cylinders as an effective medium, they found an analytical formulation for both reflection and transmission coefficients for the semi-infinite arrays of cylinders. In this research, WAMIT, a radiation/diffraction panel program developed to analyze the interaction between surface waves and offshore structures, is used to study the interactions between waves and arrays of cylinders. Results from WAMIT and Hu and

---

This thesis follows the style of Ocean Engineering.

Chan (2005) are then compared to each other to show similarity between them and validate WAMIT's output.

However, the formulation of Hu and Chan (2005) seems to be incomplete in describing the behavior of infinitely long, finite width cylinder arrays, as inferred from the Fabry-Pérot interferometer, which is an optical device. Through extensive analysis using WAMIT, it is shown that Fabry-Pérot interferometer theory can explain the interaction of long waves with finite width cylinder arrays as long as the effective array width is properly determined.

Moreover, in acoustics, it is well-known that, for certain frequencies, sound is attenuated while it propagates through a layer of bubbly liquid. Can an analogous phenomenon exist for the case of a long wave propagating through an array of vibrating cylinders? Junger and Cole (1980) and Commander and Prosperetti (1989) investigated the propagation and the attenuation of sound through a cloud of bubbles in a liquid. They also defined reflection and transmission coefficients for the bubbly layer. One of the objectives of this research is to use WAMIT to calculate reflection and transmission coefficients and to investigate whether acoustical analogies are evident for wave interactions with an array of flexible cylinders.

1.2 Literature review

A lot of work has been devoted to wave scattering by cylinders and cylinder arrays. The first order scattering velocity potential for a single cylinder is well known. The analytical solution was formulated by MacCamy and Fuchs (1954). The second and higher order solutions received more attention and semi-analytical solutions have been described by Kim and Yue (1989) and Eatock Taylor and Huang (1997). However the present thesis only focuses on the first order diffraction potential.

Additionally, wave scattering by arrays of both bottom-mounted and floating circular cylinders have received particular attention. In fact offshore structures such as tension-legs platform, floating airport or floating bridges may be modeled by arrays of floating or bottom-mounted cylinders. For example Evans and Porter (1997), Mclver (2002) and Walker and Eatock Taylor (2005) investigated wave trapping in an array of bottom-mounted cylinders. Siddorn and Eatock Taylor (2008) studied radiation and diffraction of linear waves by arrays of truncated, floating cylinders which were free to oscillate individually. Solutions for the radiated and diffracted waves, the exciting forces, the added mass and the damping for each cylinder of the array have been analytically formulated.

From the point of view of investigations of optical analogies, Hu an Chan (2005) have formulated an effective water medium approach which is applied to an array of bottom-mounted cylinders. As explained in the previous section, they defined reflection

and transmission coefficients for the array. The theory behind the effective water medium approach is described in section 2.

The motivation and the main objective of this study is to analyze wave interactions with arrays of flexible cylinders. In order to investigate analogies with wave attenuation phenomena, which occur in the acoustic problem when an acoustic wave crosses a bubble swarm, the studied cylinder should present similar deformation behavior as bubbles. Hence, the case of a cylinder which can have radial "breathing" deformation modes is studied. The theory of shell vibration may be used to describe the equations of motion. Leissa (1973) regrouped all the main theories associated with vibration of thin shells. One of them, the Donnell and Mushtari theory, is used in this research and is described in section 3. The equations of motion from Donnell and Mushtari are derived from the basic theory of surfaces and the strain-displacement equations using Love's first approximation based on four assumptions. The equations of motion may be written as a system of three equations depending on a vector of displacement and a Donnell-Mushtari operator, which can be modified if eighth order shell theories such as Love-Timoshenko, Goldenveizer-Novozhilov and Houghton-Johns are considered. The displacements can be decomposed in different modes in the vertical, tangential and radial directions.

The Donnell and Mushtari equations have been used by Sorokin and Ershova (2006) to describe the free vibration of elastic cylindrical shells with and without internal fluid. The paper studied the transmission of vibroacoustic energy in pipelines. It is

shown by both theory and experimental studies that the highest vibroacoustic energy may be attributed to the breathing mode, which is the lowest order mode.

Newman (1994) discussed the wave effects on deformable bodies. If the motions of floating bodies are usually described by six rigid body modes, additional modes called generalized modes can be added to study structural deflections. Newman developed a method to study separately the radiation potentials associated with the different modes. He also defined mass and stiffness matrices as well as added-mass and damping coefficients. He gave two examples of application for this method. The first one concerns the bending of a slender barge and the second one describes a bending vertical column where Jacobi polynomials are used to characterize the bending modes. These modes have been incorporated into the WAMIT subroutine called NEWMODES. The method used by Newman to define mass and stiffness matrices is explained in section 3.

The investigation of the analogy between an acoustical problem and the interaction between waves and an array of elastic cylinders is based on two papers. The first one is from Commander and Prosperetti (1989) which presents a model for the propagation of pressure waves in a bubbly liquid. This model had been formulated by Van Wijngaarden (1968). It used an effective medium approach allowing the definition of transmission coefficients from the bubbly layer as well as an attenuation coefficient for the transmitted wave. The model also considers bubbles dynamics. In fact, the radial motion of a bubble was formulated by Keller (1953).

The other paper related to the analogy with an acoustical problem is from Junger and Cole (1980). They studied sound propagation in a bubble swarm. The analyzed

system is a point-excited plate radiating through a layer consisting of air bubbles in an ambient liquid. They theoretically determined a complex wavenumber for a distribution of bubble sizes, which characterizes the propagation of the sound. A resonance frequency associated with each bubble size is identified, as well as an antiresonance frequency which occurs at a higher frequency. At the antiresonance frequency the bubble swarm medium is effectively incompressible and acoustic wave propagation becomes impossible. In addition, the Insertion Loss (IL) of a bubble swarm is discussed and it is found to be more effective at and above the bubble resonance. The Insertion Loss is a measure of the attenuation. In acoustics it is usually expressed in dB and is defined as $IL = 20\ log\left|{p_r}/{p_w}\right|$ where p_r is the pressure radiated by the bubble swarm and p_w is the pressure transmitted into the bubble swarm. This definition of the Insertion Loss will be applied in the case studied in this research, where the bubble swarm will be replaced by an array of elastic cylinders and the acoustic wave by a water wave.

1.3 WAMIT's inputs

WAMIT is a radiation/diffraction panel program developed to analyze the interaction between surface waves and large displacement bodies.

Two subprograms are run by WAMIT. The first one is the subprogram POTEN. Input files to this program include wave periods, water depth, wave heading angles and the geometry of the body which is defined in the Geometric Data File (GDF). The second one is the subprogram FORCE. The input files to FORCE include the body dynamic parameters (mass, external damping, external stiffness) and are specified in the Force Control File (FRC). POTEN solves the radiation and diffraction velocity potentials. FORCE is a post-processor for determining hydrodynamic coefficients, field pressures, free surface elevations, RAOs, etc.

1.3.1 Geometry of the body

Two options may be used to define the geometry of the body : the low-order method and the high-order method. When the low-order method is used, the body is discretized by a set of flat panel and the Cartesian coordinates of each panel of the body have to be defined.

For this study the high-order method has been used. The body surface is defined by patches where the Cartesian coordinates of the points on each patch are defined by mapping functions. The advantage of this method is that for one patch, the surface is smooth with continuous coordinates and slope.

Moreover, planes of symmetry can be used to limit the computational time. In this research a circular cylinder is studied with vertical planes X = 0 and Y = 0 as planes of symmetry.

Low-order and high-order method also relates to how the velocity potential is represented. In fact, in high-order method, the velocity potential is represented by b-splines in a continuous manner. With the same number of unknowns, the high-order method provides a more accurate representation of the spatial variation of the velocity potential.

The geometry of the body is analytically defined in the GEOMXACT file in WAMIT and in the present case, the subroutine CIRCCYL has been used and it only requires draft and radius of the cylinder as inputs.

1.3.2 Single and multiple bodies

For the case of diffraction by an array of rigid circular cylinders, the entire array has been considered as a single body with X = 0 and Y = 0 planes of symmetry.

For an array of independently radiating elastic cylinders, each cylinder has to be considered as one body. Then a multiple body analysis is applied.

1.3.3 Generalized body modes

To analyze the wave interaction with a deformable structure, generalized body modes corresponding to the deformations have to be incorporated into WAMIT. WAMIT's NEWMODES subroutine can then be modified to add these new modes.

1.3.4 Processing of WAMIT results

MATLAB has been used to process WAMIT's results. Codes have been written to plot surface elevations for the different cases that have been run with WAMIT and to determine reflection and transmission coefficients for the arrays. The method applied to determine these coefficients is described in section 2.

1.4 Outline of thesis

This thesis consists of four sections. The present one describes the motivation for the research, reviews the relevant literature and summarizes the software WAMIT which has been used to analyze the interactions between water waves and arrays of cylinders.

The second part of this thesis recapitulates the theory of scattering by a single rigid bottom-mounted cylinder, formulated by MacCamy and Fuchs (1954), and compares these results with those obtained using WAMIT in order to verify the consistency of WAMIT's results using the high-order method. Then, the effective water medium approach is formulated according to previous work by Hu and Chan (2005). Using the effective medium approach, the interaction between a wave train and an array of vertical cylinders can be described using laws or properties from optics such as Snell's law and Fabry-Pérot interferometry. Results from WAMIT will be presented, discussed and related to the effective water medium approach. The last part of this section will study the particular case of a bi-convex array of cylinders which has wave energy focusing properties.

The objective of the third section is to study the case of an elastic bottom-mounted cylinder. The theory of vibrating shells used to determine the equations of motion of the elastic cylinder will be described. The generalized modes that have to be incorporated into WAMIT's subroutine will be presented and WAMIT's results for a single elastic cylinder will be discussed.

The fourth and last section consists of a summary and conclusions of the research. It will also present some suggestions for possible future work related to this research.

2. ARRAYS OF BOTTOM-MOUNTED RIGID CYLINDERS

The first part of this thesis recapitulates the first order diffraction potential and surface elevation from MacCamy and Fuchs (1954) theory for a bottom-mounted rigid cylinder. Then the case of a regular array of these cylinders will be studied.

The effective medium approach according to Hu and Chan (2005) is described in the following section and the same cases as Hu and Chan (2005) have been run with WAMIT. WAMIT's results show certain phenomena which are evoked but not fully described by Hu and Chan (2005). These include the Fabry-Pérot interferometer effects. From the theory associated with the Fabry-Pérot Interferometer, which is an optical device, it is possible to derive an analytical formulation for the reflectance and the transmittance of an array of cylinders taking into account the multiple reflection occurring in the array.

These results are compared with WAMIT's output, and some inconsistencies will lead to the definition of an effective width for the array. The maximum likelihood method used to calculate reflectance and transmittance from WAMIT's output will be also presented in this section.

The last section is devoted to a bi-convex array of cylinders which presents wave energy focusing properties. WAMIT's results for this particular array are compared against basic optical theory for a converging lens, and the contribution of effective width will be also described.

2.1 Single bottom-mounted rigid cylinder

The objective of this section is to compare the MacCamy and Fuchs (1954) theory, which formulates the linear diffraction potential for a bottom-mounted cylinder, to the results obtained from WAMIT. In fact, it is the first step to validate the high-order method used to define the geometry of the body in WAMIT.

A description of the MacCamy and Fuchs formulation for the diffraction potential and wave elevation for a bottom-mounted circular cylinder is provided below. It is convenient to use cylindrical coordinates (r,θ,z) because the geometry of the system consists of a bottom-mounted rigid circular cylinder. The system is illustrated in Fig. 2.1.

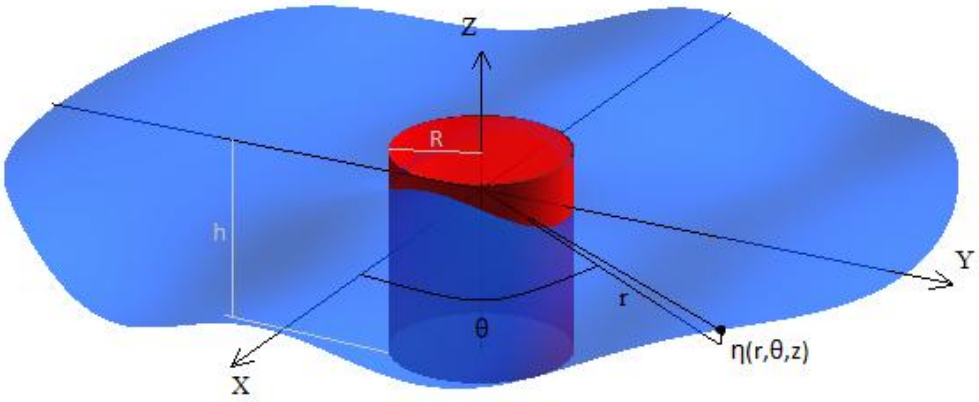

Fig. 2.1. Bottom-mounted, circular, vertical cylinder in cylindrical coordinates

The diffraction velocity potential ϕ_D can be decomposed as a combination of an incident velocity potential and a scattering velocity potential:

$$\phi_D = \phi_I + \phi_S \tag{2.1}$$

where ϕ_I is the incident potential and ϕ_S is the scattered potential.

The diffraction potential ϕ_D satisfies Laplace's equation in the fluid domain

$$\nabla^2\phi_D = \frac{\partial^2\phi_D}{\partial r^2} + \frac{1}{r}\frac{\partial\phi_D}{\partial r} + \frac{1}{r^2}\frac{\partial^2\phi_D}{\partial\theta^2} + \frac{\partial^2\phi_D}{\partial z^2} = 0 \quad \text{in the fluid domain} \tag{2.2}$$

and the following boundary conditions:

$$\frac{\partial\phi_D}{\partial z} = 0 \qquad \text{on } z = -h \tag{2.3}$$

$$\frac{\partial\eta}{\partial t} - \frac{\partial\phi_D}{\partial z} = 0 \qquad \text{on } z = 0 \tag{2.4}$$

$$\frac{\partial\phi_D}{\partial t} + g\eta = 0 \qquad \text{on } z = 0 \tag{2.5}$$

$$\frac{\partial\phi_D}{\partial r} = \frac{\partial\phi_I}{\partial r} + \frac{\partial\phi_S}{\partial r} = 0 \qquad \text{on } r = R \tag{2.6}$$

Far away from the cylinder, ϕ_S should satisfy the Sommerfeld radiation condition:

$$\lim_{r\to\infty}\sqrt{r}\left\{\frac{\partial\phi_S}{\partial r} - ik\phi_S\right\} = 0 \tag{2.7}$$

where η is the wave elevation and k the wavenumber.

In cylindrical coordinates e^{ikx} can be rewritten as:

$$\begin{aligned} e^{ikx} &= \cos(kx) + i\,sin(kx) = \cos(krcos\theta) + i\sin(krcos\theta) \\ &= \sum_{n=0}^{\infty}\varepsilon_n J_n(kr)\cos(n\theta) \end{aligned} \tag{2.8}$$

where J_n is the first kind Bessel function of order n and ε_n is a coefficient having the following expression:

$$\varepsilon_n = \begin{cases} 1 & \text{for } n = 0 \\ 2i^n & \text{for } n > 0 \end{cases} \tag{2.9}$$

The solution for the first-order incident potential in cylindrical coordinates is given by:

$$\phi_I = -i\frac{gA}{\omega}\frac{cosh(k(z+h))}{cosh(kh)}\left\{\sum_{n=0}^{\infty}\varepsilon_n J_n(kr)\cos(n\theta)\right\}e^{-i\omega t} \tag{2.10}$$

where A is the amplitude of the incident wave, g is the gravitational acceleration and ω is the angular frequency of the incident wave.

The solution for the first-order scattered wave potential is given by:

$$\phi_s = i\frac{gA}{\omega}\frac{cosh(k(z+h))}{cosh(kh)}\left\{\sum_{n=0}^{\infty}\varepsilon_n \frac{J_n'(kR)}{H_n'(kR)} H_n(kr)\cos(n\theta)\right\}e^{-i\omega t} \tag{2.11}$$

where H_n is the Bessel function of the third kind (Hankel function).

Therefore, the first-order diffracted wave is:

$$\phi_D = i\frac{gA}{\omega}\frac{cosh\big(k(z+h)\big)}{cosh(kh)}\sum_{n=0}^{\infty}\varepsilon_n\left(\frac{J_n'(kR)}{H_n'(kR)} H_n(kr) - J_n(kr)\right)\cos(n\theta)\, e^{-i\omega t} \tag{2.12}$$

and the first order surface elevation is:

$$\eta = A\left\{\sum_{n=0}^{\infty}\varepsilon_n\left(J_n(kr) - \frac{J_n'(kR)}{H_n'(kR)} H_n(kr)\right)\cos(n\theta)\right\}e^{-i\omega t} \tag{2.13}$$

The analytical solution for the free surface elevation was coded in MATLAB and used to generate results for comparison with WAMIT. Fig. 2.2 represents the diffracted wave elevation corresponding to unit amplitude incident waves. Bessel's function

defined in MATLAB have been used. The geometrical parameters used to plot Fig. 2.2 are recapitulated in Table 2.1.

Table 2.1. Parameters used in WAMIT for the single bottom-mounted cylinder

Parameter	Value
Radius of cylinder, R	17.5 ft
Draft of cylinder, d	40 ft
Water depth, h	40 ft
Wave period, T	7.99 sec
Amplitude of incident wave, A	1
Gravitational acceleration, g	32.2 ft/s^2
Scatter parameter, kR	0.440

Fig. 2.3 illustrates the wave elevation corresponding to the diffraction potential obtained from WAMIT. Fig. 2.4 compares the wave elevation computed by MacCamy-Fuchs and WAMIT along the two perpendicular transects through the cylinder, and it can been seen that the results are practically indistinguishable. The excellent agreement demonstrated in Fig. 2.3 and Fig. 2.4 validates our implementation of the high-order method in WAMIT.

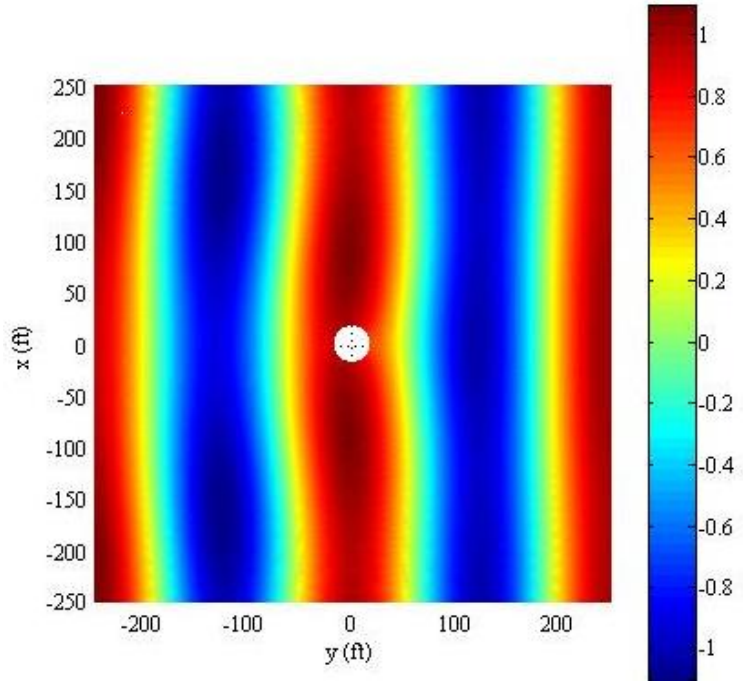

Fig. 2.2. Wave elevation for a bottom-mounted, rigid, circular cylinder from MacCamy and Fuchs theory.

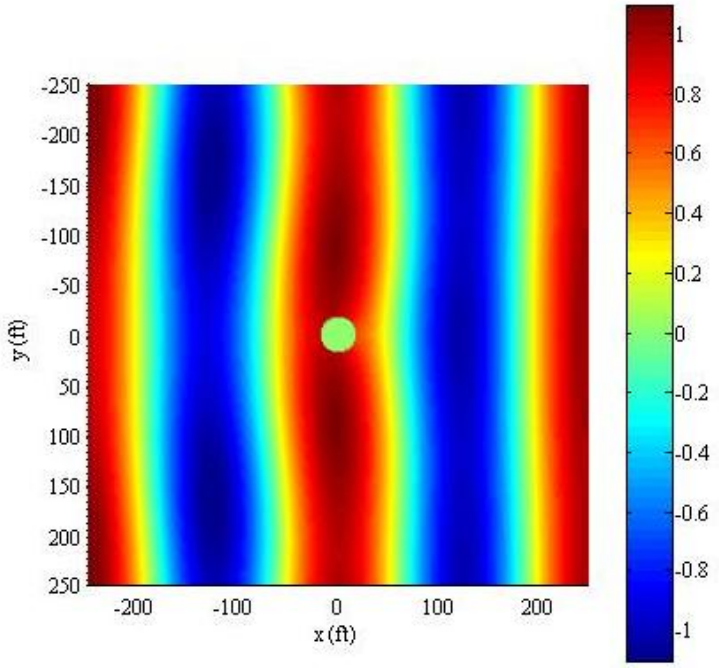

Fig. 2.3. Wave elevation for a bottom-mounted, rigid, circular cylinder from WAMIT surface elevation outputs.

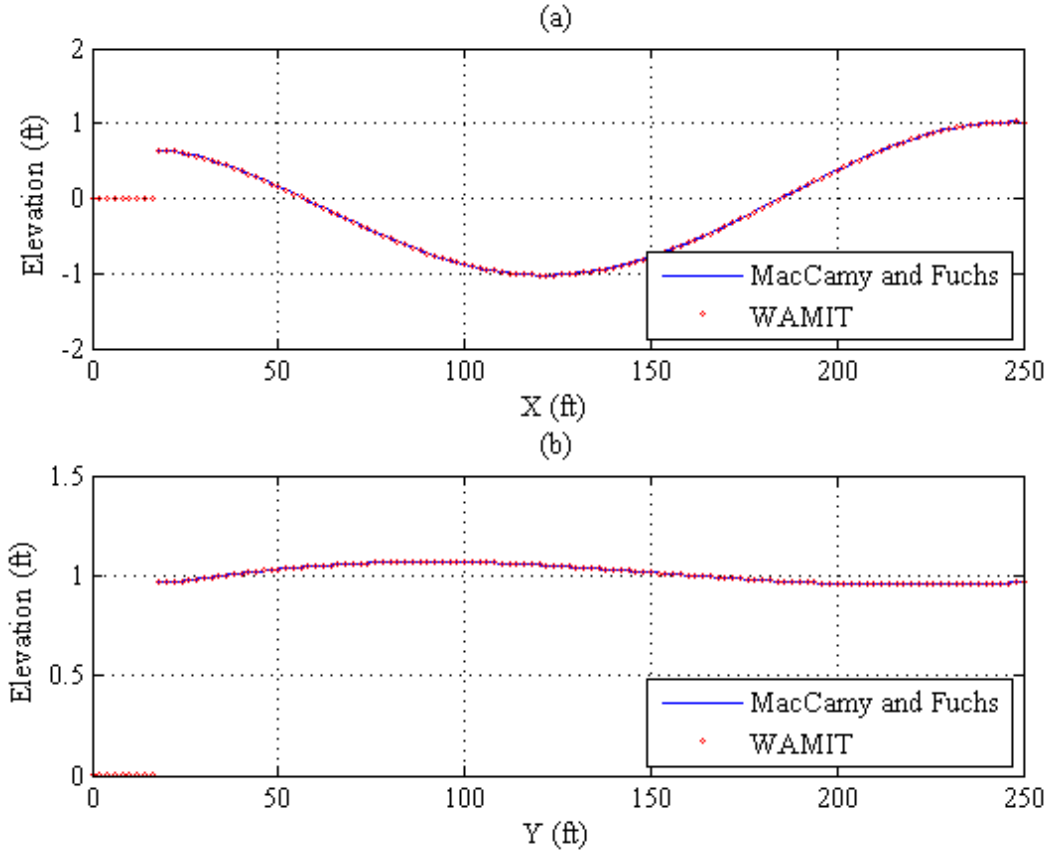

Fig. 2.4. Comparison between MacCamy and Fuchs theory and WAMIT surface elevation in x-direction and y-direction. Both figures show good agreement between theory and WAMIT results.

2.2 Effective water medium approach

In order to investigate the optical analogies to the interaction between long waves and an array of cylinders, an effective water medium approach developed by Hu and Chan (2005) is used. A regular spaced array of cylinders is considered as an effective medium. Depth, gravitational acceleration and wavenumber inside this effective medium are different from those outside the medium. Moreover, the size of the medium (defined by the parameter a) is chosen so that scattering waves outside the medium may be neglected.

The formulation of the effective parameters inside the medium such as depth, wavenumber and gravitational acceleration are found by reasoning on a single cylinder. An area (zone B) around each cylinder is defined as illustrated in Fig. 2.5. In zone B the wavenumber k_e is different from the wavenumber k in zone A. More precisely, zone B has a surface equal to a^2. It can be defined either as a square of surface a -by- a or as a circle of radius R_e which has a surface of a^2 around each cylinder of radius R. Moreover, the effective medium in Zone B has a water depth h_e and a gravitational acceleration g_e while Zone A has a water depth h and a gravitational acceleration g.

If not only one cylinder is considered but an array of cylinders, the distance between these cylinders is set to be equal to a. Therefore, the whole array may be considered as an effective medium in which the wave propagates with an effective wavenumber k_e, an effective water depth h_e and an effective gravitational acceleration g_e.

A filling ratio f_s of the medium can be formulated as:

$$f_s = \frac{\text{volume of cylinder}}{\text{volume of medium}} = \frac{\pi R^2}{a^2} \tag{2.14}$$

If an array of N cylinders is now considered, the same definition for the filling ratio may be applied:

$$f_s = \frac{N\pi R^2}{Na^2} = \frac{\pi R^2}{a^2}$$

This definition of the filling ratio is the main parameter which characterizes the array of cylinders and it will be used in the formulation of reflection and transmission coefficients by the array.

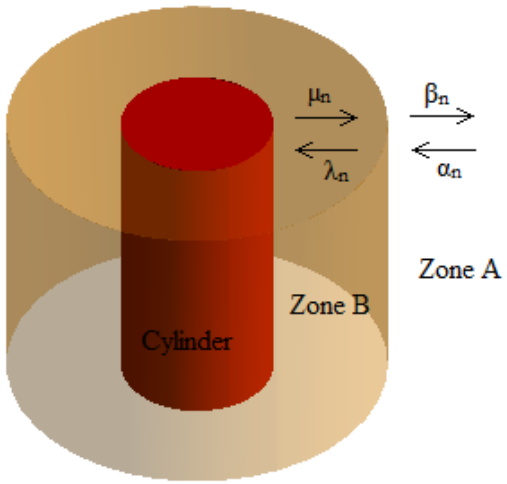

Fig. 2.5. Effective water medium (zone B) around a circular cylinder of radius R, bottom-mounted in water (zone A). $\alpha_n$and β_n are the amplitudes of respectively the incident and scattering waves in zone A and λ_n and μ_n are the amplitudes of respectively the incident and scattering waves in zone B

The following paragraphs describe how the effective parameters, such as the effective depth, the effective gravitational acceleration and the effective wavenumber, are obtained considering only one single cylinder surrounded by the effective medium. Then, these effective parameters may be generalized to the whole array of cylinders if the distance between the cylinders correspond to the dimension a of the effective medium surrounding one cylinder.

Considering a harmonic long water wave of frequency ω, the displacement of the surface η follows the two dimensional Helmholtz equation:

$$(\nabla^2 + k^2)\eta = 0 \tag{2.15}$$

where k is the wavenumber derived from the dispersion relation

$$\omega^2 = gk\tanh(kh) \tag{2.16}$$

Considering shallow water ($kh << 1$), the dispersion relation becomes

$$\omega^2 = ghk^2 \tag{2.17}$$

At the surface of the cylinder, the following boundary condition implies no flow through the cylinder:

$$\frac{\partial \eta}{\partial \vec{n}} = 0 \tag{2.18}$$

where $\vec{n}$ is the normal vector to the surface of the cylinder.

Substituting equation (2.17) into equation (2.15), the Helmholtz equation becomes

$$\mathrm{h}\nabla^2\eta + \frac{\omega^2}{\mathrm{g}}\eta = 0 \tag{2.19}$$

The solution of equation (2.19) in terms of surface elevation can be written as a linear combination of first kind Bessel functions and Hankel functions.

In zone A, outside the effective medium, the wave elevation η_A can be written as

$$\eta_A = \sum_{n=0}^{\infty} \left(\alpha_n J_n(kr) + \beta_n H_n(kr)\right) e^{in\theta} \tag{2.20}$$

And in zone B, in the effective medium, the wave elevation η_B has the form:

$$\eta_B = \sum_{n=0}^{\infty} \left(\lambda_n J_n(k_e r) + \mu_n H_n(k_e r)\right) e^{in\theta} \tag{2.21}$$

The Bessel function J_n corresponds to the incident wave with corresponding amplitudes α_n in zone A and λ_n in zone B, while the Hankel function H_n corresponds to the scattering wave with associated amplitudes β_n in zone A and μ_n in zone B.

Continuity in surface elevation between zone A and zone B leads to the relation

$$\eta_A(R_e) = \eta_B(R_e) \tag{2.22}$$

which can be rewritten as

$$\alpha_n J_n(kR_e) + \beta_n H_n(kR_e) = \lambda_n J_n(k_e R_e) + \mu_n H_n(k_e R_e) \tag{2.23}$$

The boundary condition on the surface of the cylinder gives:

$$\frac{\partial \eta_B(R)}{\partial r} = 0 \tag{2.24}$$

which may be written as

$$k_e \lambda_n J_n'(k_e R) + k_e \mu_n H_n'(k_e R) = 0 \tag{2.25}$$

and the continuity in flow between zone A and zone B leads to:

$$h \frac{\partial \eta_A(R_e)}{\partial r} = h_e \frac{\partial \eta_B(R_e)}{\partial r} \tag{2.26}$$

which can be expressed as

$$h\{k\alpha_n J_n'(kR_e) + k\beta_n H_n'(kR_e)\} = h_e\{k_e \lambda_n J_n'(k_e R_e) + k_e \mu_n H_n'(k_e R_e)\} \tag{2.27}$$

The effective medium is defined so that scattering waves do not exist outside the medium in zone A. If the total array of cylinders is considered as an effective medium, the result is that the waves become macrocosmically planar in the array of cylinders (see figure on page 37) and that allows the definition of a refracted wave inside the array. Therefore, in equations (2.23), (2.25) and (2.27), the scattering coefficient β_n is set to 0. The combination of equations (2.23), (2.25) and (2.27) leads to:

$$\begin{aligned} -hkJ_n(k_eR_e)\{H_n^{'}(kR)J_n^{'}(kR_e) - H_n^{'}(kR_e)J_n^{'}(kR)\} \\ + h_ek_eJ_n^{'}(k_eR_e)\{H_n^{'}(kR)J_n(kR_e) - H_n(kR_{e)})J_n^{'}(kR)\} \\ = 0 \end{aligned} \tag{2.28}$$

When ka<<1, Bessel and Hankel functions may be simplified and the following relations are verified:

$$k_e^2h_e = (1 - f_s)hk^2 \qquad \text{for } n = 0 \tag{2.29}$$

$$h_e = h\frac{(1 - f_s^n)}{(1 + f_s^n)} \qquad \text{for } n > 0 \tag{2.30}$$

Besides, in shallow water, the wavenumbers may be expressed as:

$$k_e = \frac{\omega}{\sqrt{g_eh_e}} \tag{2.31}$$

$$k = \frac{\omega}{\sqrt{g\,h}} \tag{2.32}$$

and for $n = 0$ and $n = 1$ equations (2.29) and (2.30) can be written as:

$$g_e = \frac{1}{1 - f_s}g \tag{2.33}$$

$$h_e = h\frac{(1-f_s)}{(1+f_s)} \tag{2.34}$$

Combining equations (2.33) and (2.34), the wavenumber k_e inside the medium can be expressed as:

$$k_e = \sqrt{1+f_s}\,k \tag{2.35}$$

and the refractive index n_e can be defined as:

$$n_e = \sqrt{1+f_s} \tag{2.36}$$

This refractive index is generalized to the whole array and is used to determine the refractive angle φ, shown in Fig. 2.6 for the semi-infinite array, using Snell's law:

$$\sin\theta = n_e \sin\varphi \tag{2.37}$$

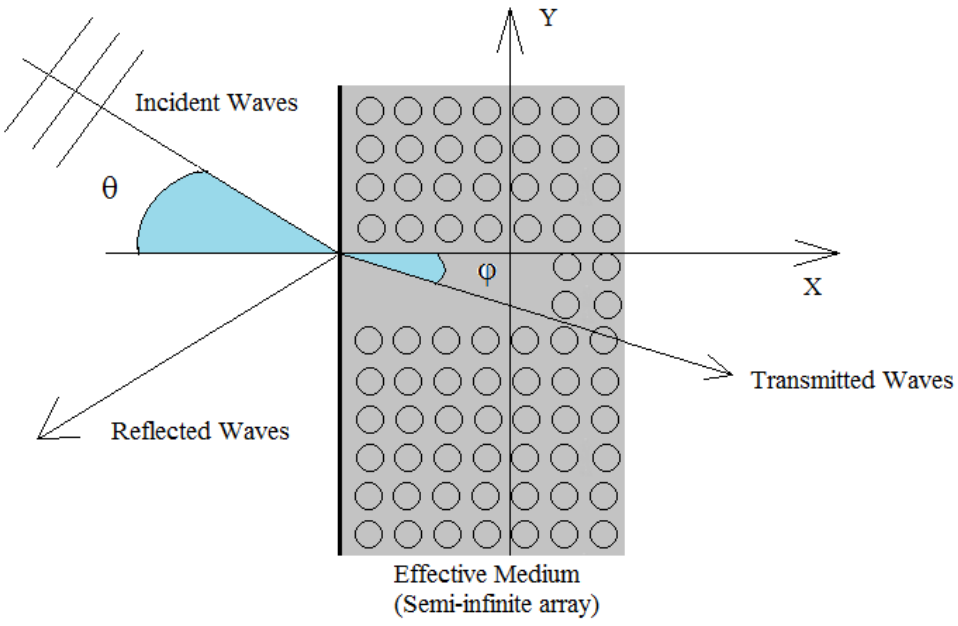

Fig. 2.6. Representation of the semi- infinite array of cylinders as an effective medium. The refractive angle φ is determined using Snell's law.

The continuity equation between waves inside and outside the medium gives

$$k = k\, r_e + \ k_e\, t_e \tag{2.38}$$

where r_e is the reflection coefficient and t_e is the transmission coefficient.

The conservation of energy may be expressed as:

$$r_e^2 + t_e^2 = 1 \tag{2.39}$$

Combining equations (2.38) and (2.39) leads to the following expressions for r_e and t_e:

$$r_e = \frac{\cos\theta - \frac{1 - f_s}{\sqrt{1 + f_s}}\cos\varphi}{\cos\theta + \frac{1 - f_s}{\sqrt{1 + f_s}}\cos\varphi} \tag{2.40}$$

$$t_e = \frac{2\cos\theta}{\cos\theta + \frac{1 - f_s}{\sqrt{1 + f_s}}\cos\varphi} \tag{2.41}$$

These are analytical expressions for reflection and transmission coefficients. Reflectance and transmittance can then be found by taking the square root of r_e and t_e.

The angle θ_0 leading to a non-reflection is called the Brewster angle and

$$\theta_0 = \arccos\left(\frac{1 - f_s}{2}\right) \tag{2.42}$$

However, these formulations of r_e and t_e only correspond to a semi-infinite array. In the finite width array case, multiple reflections and transmissions inside the array have to be considered. This is why reflection and transmission coefficients formulated in equation (2.40) and (2.41) have to be combined with the theory associated with the Fabry-Pérot interferometer. The next section describes the theory for the Fabry-Pérot interferometer.

2.3 Fabry-Pérot interferometer

The Fabry-Pérot interferometer is an optical device used to measure the wavelength of light. It consists of two transparent plates with reflecting surfaces. The density of the medium between these two surfaces is different from the density of the medium outside the plates.

The theory associated to the Fabry-Pérot Interferometer is used in our case to predict reflectance and transmittance for the array of cylinders. The following paragraph presents the theory associated with the Fabry-Pérot Interferometer which is illustrated in Fig. 2.7.

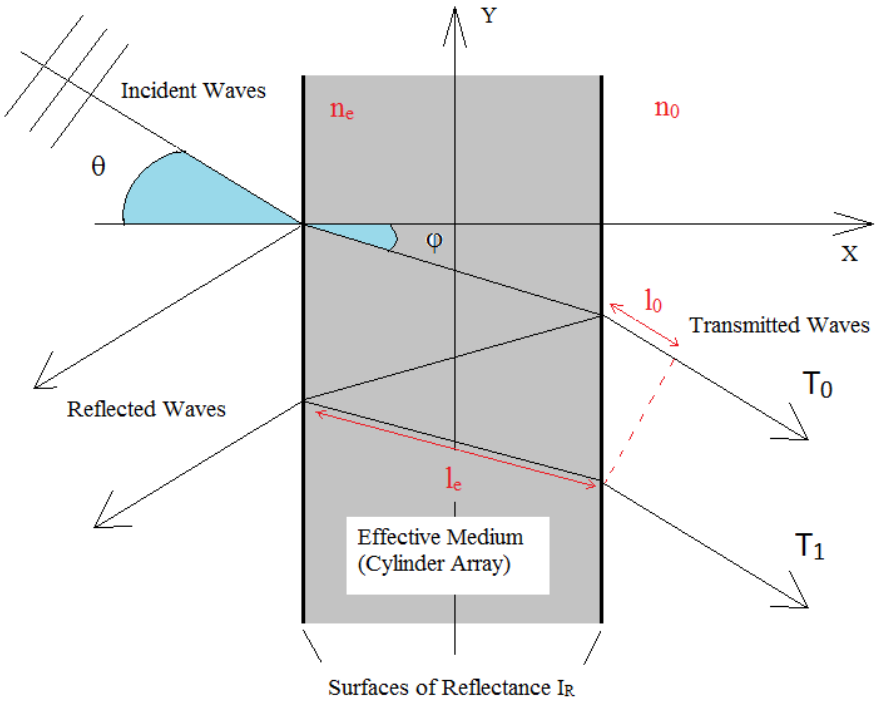

Fig. 2.7. Fabry-Pérot interferometer constituted of reflecting surfaces. Multiple reflection and transmission occur inside the medium.

In this section t and r are respectively the complex-valued transmitted and reflected wave amplitude coefficients associated with the interferometer and T and R are respectively the transmitted and reflected intensities (transmittance and reflectance) associated with the interferometer. T and R may be expressed as:

$$T = t^2 \tag{2.43}$$

$$R = r^2 \tag{2.44}$$

$$T + R = 1 \tag{2.45}$$

A beam of unit amplitude is incident from infinity to the first plate (plate 1). A part of it is reflected by plate 1 and the other part is transmitted to the inner medium. The transmitted beam in the inner medium has now an amplitude t. When it meets the second plate (plate 2), one part is transmitted to the outside and another is reflected by plate 2 back to the inner medium. The transmitted one has an amplitude $t \times t$ but a phase lag for the path in the inner medium has to be added : $e^{ik_e l_e}$. Hence, the first transmitted wave is

$$T_0 = t^2 e^{ik_e l_e} = T e^{ik_e l_e} \tag{2.46}$$

The second transmitted wave may be similarly derived, but it is necessary to add a phase lag $e^{-ik_0 l_0}$ to account for the lag between T_0 and T_1 , and because the beam has crossed the medium three times, the corresponding phase lag becomes $e^{3ik_e l_e}$ (lengths l_e and l_0 are represented in Fig. 2.7). Thus T_1 is represented by the following expression:

$$T_1 = tr^2 t\left(e^{3ik_e l_e} e^{-ik_0 l_0}\right) = TR e^{3ik_e l_e - ik_0 l_0} \tag{2.47}$$

Therefore, using Snell's law, the total phase difference between the two beams is:

$$\delta = 2k_e l_e - k_0 l_0 = 2ek_e \cos\varphi \tag{2.48}$$

More generally, the n[th] transmitted beam has an amplitude:

$$T_n = TR^n e^{in\delta} \tag{2.49}$$

Then, the total transmitted amplitude is:

$$A_T = \sum_{n=0}^{\infty} T_n = T \sum_{n=0}^{\infty} \left(Re^{i\delta}\right)^n \tag{2.50}$$

Because $Re^{i\delta} < 1$, A_T can be rewritten as:

$$A_T = \frac{T}{1 - Re^{i\delta}} \tag{2.51}$$

The transmitted intensity is defined as:

$$I_T = A_T A_T^* = \frac{(1-R)^2}{1 + R^2 - 2R\cos\delta} \tag{2.52}$$

and the reflected intensity as:

$$I_R = 1 - I_T = 1 - \frac{(1-R)^2}{1 + R^2 - 2R\cos\delta} \tag{2.53}$$

The last expression (I_R) is used for the comparison with WAMIT's results. One can observe that this expression depends on the width of the medium which will have to be defined. Moreover, for certain values of δ and consequently for certain values of θ, equation (2.53) is equal to zero which leads to a non-reflection from the array. These values for the incident angles are different from the Brewster angle discussed in section 2.2.

The next section explains how the reflection and transmission coefficients from WAMIT's surface elevation outputs have been determined.

2.4 Method to determine reflection coefficients from WAMIT

2.4.1 Decomposition of the wave elevation domain

WAMIT returns the wave elevation for the input grid of free surface field points. The grid specified in the FORCE input file has a spacing of 5 ft. As shown in Fig. 2.8., the array is 10000 ft long in WAMIT, long enough to avoid sides effects. In fact for higher headings (e.g. 80 deg), the transmitted wave is more affected by the end effects. The studied part is 1500 ft long and 3000 ft wide. The cylinder array is constituted of 9 layers and the distance between the cylinders is 50 ft.

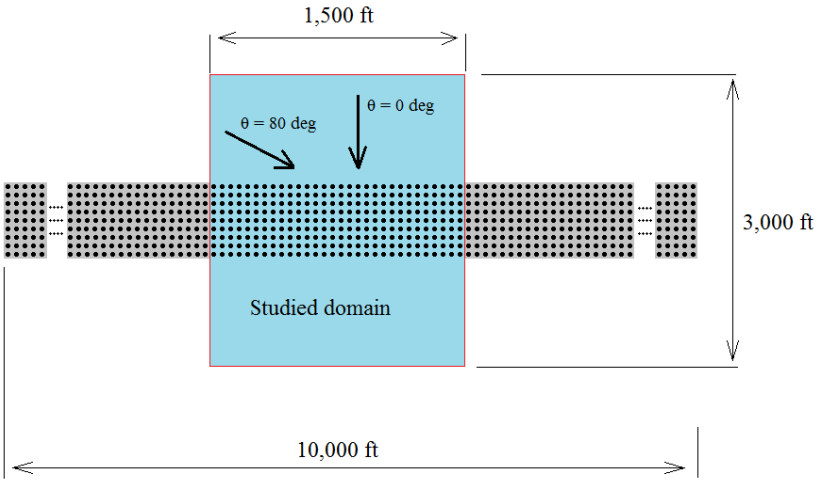

Fig. 2.8. Array of cylinders. The blue zone is the studied domain.

In order to study wave elevation, the field the separated into three domains as illustrated in Fig. 2.9.

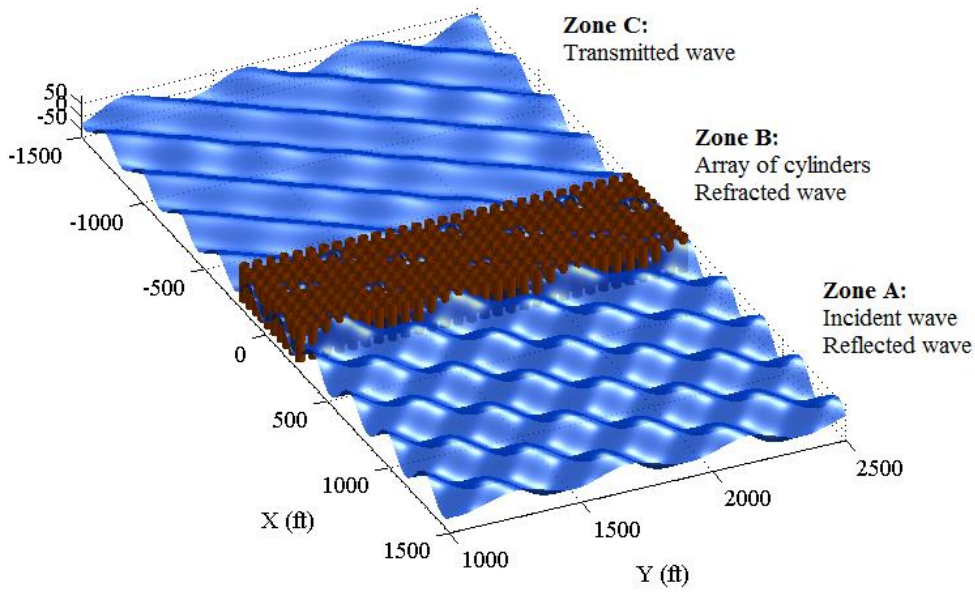

Fig. 2.9. Decomposition of the studied domain into three zones. Zone A contains incident and reflected waves, zone B is the array of cylinder containing a refracted wave and Zone C contains a transmitted wave.

The first zone is the incident domain (zone A) which contains an incident wave and a reflected wave from the reflection with the array.

The incident wave elevation is defined as

$$\eta_{I,1}(x,y) = K_{I,1}\cos\big(k\,(x\cos\theta - y\sin\theta)\big) \tag{2.54}$$

The reflected wave elevation is defined as

$$\eta_{R,1}(x,y) = K_{R,1}\cos\big(k\,(x\cos\theta + y\sin\theta) + \varepsilon_{R,1}\big) \tag{2.55}$$

The total wave elevation is therefore

$$\eta_1(x,y) = \eta_{I,1}(x,y) + \eta_{R,1}(x,y) \tag{2.56}$$

The second zone is the array of cylinders (zone B) and the effective water medium which contains two waves.

A transmitted wave from the incident domain to the array

$$\eta_{T,2}(x,y) = K_{T,2}\cos\left(k_e\,(x\cos\varphi - y\sin\varphi) + \varepsilon_{T,2}\right) \tag{2.57}$$

A reflected wave from the second edge of the array

$$\eta_{R,2}(x,y) = K_{R,2}\cos\left(k_e\,(x\cos\varphi + y\sin\varphi) + \varepsilon_{R,2}\right) \tag{2.58}$$

Thus, the total wave elevation is

$$\eta_2(x,y) = \eta_{T,2}(x,y) + \eta_{R,2}(x,y) \tag{2.59}$$

Due to refraction, the transmitted and reflected waves inside the array propagate with angle $\pm\varphi$.

The third zone is the transmitted domain (zone C) that only contains the transmitted wave from the array.

$$\eta_{T,3}(x,y) = K_{T,3}\cos\left(k\,(x\cos\theta - y\sin\theta) + \varepsilon_{T,3}\right) \tag{2.60}$$

And the total wave elevation is

$$\eta_3(x,y) = \eta_{T,3}(x,y) \tag{2.61}$$

2.4.2 The Maximum Likelihood Method

The Maximum Likelihood Method (MLM), which is a statistical method, has been used to determine reflection and transmission coefficients for the three parts of the field. The MLM is computationally efficient and robust because it requires a few numbers of outcomes and it avoids accumulation of numerical errors.

The measured or calculated data can be decomposed as:

$$Y_i = X_{ij} a_j + e_i \tag{2.62}$$

where $X_{ij} a_j$ represents the linear harmonic response, e_i is the error, $i = [1:n]$ are the time steps and $j = 1,2,\dots,K$ where K is the number of unknowns. The unknown parameters are included in a_j.

In matrix notation,

$$\{Y\} = [X]\{a\} + \{e\} \tag{2.63}$$

Then $\{a\}$ is obtained as

$$\{a\} = ([X]^T[X])^{-1}[X]^T\{Y\} \tag{2.64}$$

In the present study, Y_i corresponds to the wave elevation data set from WAMIT and $X_{ij} a_j$ is the theoretical linear wave elevation where the unknowns are the reflected and transmitted coefficients and the phase lags induced by the reflection and transmission process.

The MLM is applied for each part of the domain defined in Fig. 2.9.

Zone A :

Only two unknowns exist in zone A: the amplitude of the reflected wave in part A, $K_{R,1}$ and its phase $\varepsilon_{R,1}$.

In that particular case, the surface wave elevation can be written as:

$$Y_i = \cos(k\,\xi_i) + K_{R,1}\cos(k\,\xi_i' + \varepsilon_{R,1}) \tag{2.65}$$

where

$$\xi_i = x_i \cos\theta - y_i \sin\theta \tag{2.66}$$

$$\xi_i' = x_i \cos\theta + y_i \sin\theta \tag{2.67}$$

Rewriting (2.65) to collect the unknowns on one side :

$$Y_i' = Y_i - \cos(k\,\xi_i) = K_{R,1}\cos(k\,\xi_i' + \varepsilon_{R,1}) \tag{2.68}$$

$$Y_i' = K_{R,1}\cos(k\,\xi_i')\cos(\varepsilon_{R,1}) - K_{R,1}\sin(k\,\xi_i')\sin(\varepsilon_{R,1}) \tag{2.69}$$

Writing equation (2.69) in terms of matrices,

$$\begin{bmatrix} Y_1' \\ Y_2' \\ \vdots \\ Y_n' \end{bmatrix} = \begin{bmatrix} \cos(k\,\xi_1') & \sin(k\,\xi_1') \\ \cos(k\,\xi_2') & \sin(k\,\xi_2') \\ \vdots & \vdots \\ \cos(k\,\xi_n') & \sin(k\,\xi_n') \end{bmatrix} \begin{bmatrix} a_1 \\ a_2 \end{bmatrix} \tag{2.70}$$

with

$$a_1 = K_{R,1}\cos(\varepsilon_{R,1}) \tag{2.71}$$

$$a_2 = K_{R,1}\sin(\varepsilon_{R,1}) \tag{2.72}$$

then the results for $K_{R,1}$ and $\varepsilon_{R,1}$ are:

$$K_{R,1} = \sqrt{a_1^2 + a_2^2} \tag{2.73}$$

$$\varepsilon_{R,1} = \arctan\left(\frac{-a_2}{a_1}\right) \tag{2.74}$$

Zone B :

In zone B there are six unknowns : $K_{T,2}$, $K_{R,2}$, $\varepsilon_{T,2}$, $\varepsilon_{R,2}$, k_e and φ where $K_{T,2}$, $K_{R,2}$ are respectively the amplitudes of the transmitted and reflected waves in zone B and $\varepsilon_{T,2}$, $\varepsilon_{R,2}$ are the phase of the transmitted and reflected waves. $K_{T,2}$, $K_{R,2}$, $\varepsilon_{T,2}$, $\varepsilon_{R,2}$ can be evaluated using the Maximum Likehood Method.

A trial-and-error procedure is used to find the k_e and φ pair that has the minimum Mean Square Error (MSE) (see Fig. 2.10).

The MLM can be set up similarly to part 1:

$$Y_i = K_{T,2}\cos\left(k_e\,\xi_i + \varepsilon_{T,2}\right) + K_{R,2}\cos\left(k_e\,\xi_i^{'} + \varepsilon_{R,2}\right) \tag{2.75}$$

Using the same decomposition for the cosine as in equation (2.69), and rewriting in term of matrices:

$$\begin{bmatrix} Y_1^{'} \\ Y_2^{'} \\ \vdots \\ Y_n^{'} \end{bmatrix} = \begin{bmatrix} \cos\left(k_e\,\xi_i\right) & \sin\left(k_e\,\xi_i\right) & \cos\left(k_e\,\xi_1^{'}\right) & \sin\left(k_e\,\xi_1^{'}\right) \\ \cos\left(k_e\,\xi_i\right) & \sin\left(k_e\,\xi_i\right) & \cos\left(k_e\,\xi_2^{'}\right) & \sin\left(k_e\,\xi_2^{'}\right) \\ \vdots & \vdots & \vdots & \vdots \\ \cos\left(k_e\,\xi_i\right) & \sin\left(k_e\,\xi_i\right) & \cos\left(k_e\,\xi_n^{'}\right) & \sin\left(k_e\,\xi_n^{'}\right) \end{bmatrix} \begin{bmatrix} a_1 \\ a_2 \\ b_1 \\ b_2 \end{bmatrix} \tag{2.76}$$

with

$$a_1 = K_{T,2}\cos\left(\varepsilon_{T,2}\right) \tag{2.77}$$

$$a_2 = K_{T,2}\sin\left(\varepsilon_{T,2}\right) \tag{2.78}$$

$$b_1 = K_{R,2}\cos\left(\varepsilon_{R,2}\right) \tag{2.79}$$

$$b_2 = K_{R,2}\sin\left(\varepsilon_{R,2}\right) \tag{2.80}$$

then

$$K_{T,2} = \sqrt{a_1^2 + a_2^2} \tag{2.81}$$

$$K_{R,2} = \sqrt{b_1^2 + b_2^2} \tag{2.82}$$

$$\varepsilon_{T,2} = \arctan\left(\frac{-a_2}{a_1}\right) \tag{2.83}$$

$$\varepsilon_{R,2} = \arctan\left(\frac{-b_2}{b_1}\right) \tag{2.84}$$

Transmission and reflection coefficients for zone C are calculated similarly to those for zone 1 since only one wave exists in that domain.

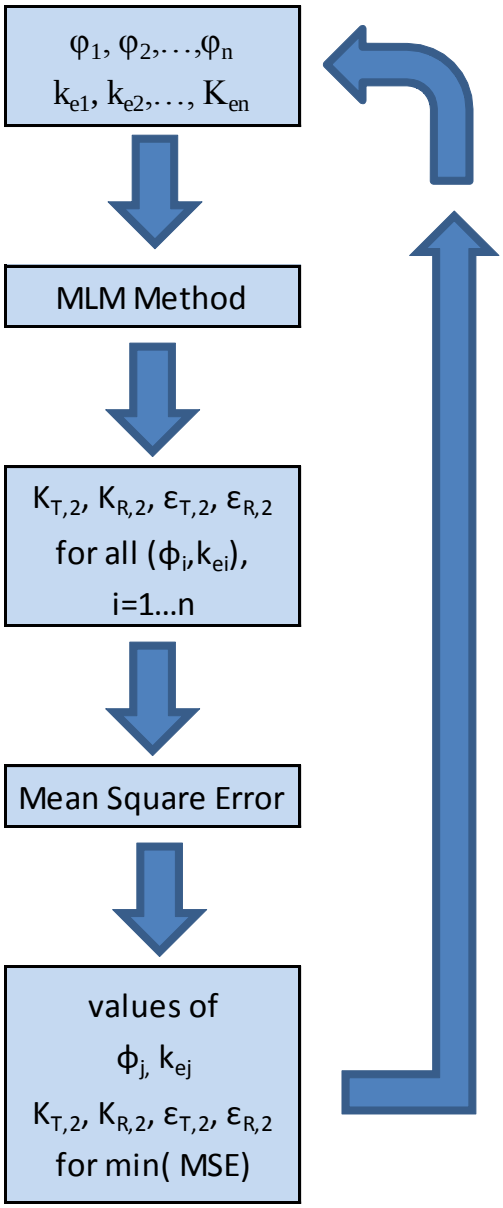

Fig. 2.10. Method to calculate reflection and transmission coefficients in zone B.

2.5 Diffraction by an array of bottom-mounted, rigid cylinders

The high-order method is used to define the geometry of the system. The body surface is defined by patches where the Cartesian coordinates of the points on each patch are defined by mapping functions. Arrays of uniformly spaced rigid cylinders are considered as one single body with two planes of symmetries in the X and Y-directions.

The completed case is a nine-layer regular array with a filling ratio equal to 0.387 for twenty different incident angles (0 to 85 degrees) and for a wave period of T = 7.99 sec. The parameters for this array are presented in Table 2.2. This is the same case studied by Hu and Chan, at least in terms of non-dimensional parameters.

The length of the array has been chosen long enough (10,000 ft) so that end effects do not dramatically affect the results for surface elevation in the central region. The length of the studied field is 1500 ft (see Fig. 2.8).

Table 2.2. Inputs used in WAMIT for the regular array of cylinders.

Parameter	Value
Radius of cylinder, R	17.5 ft
Draft of cylinder, d	40 ft
Water depth, h	40 ft
Wave period, T	7.99 sec
Wavenumber, k	$0.02513 ft^{-1}$
Amplitude of incident wave, A	1
Gravitational acceleration, g	$32.2 ft/s^2$
Filling ratio, f_s	0.385
Spacing between cylinders, a	40 ft
Length of the array	10,000 ft
Width of the array	450 ft
Number of cylinders, N	1800
Number of cylinders in X-dir., N_x	9
Number of cylinder in Y-dir., N_y	200

2.5.1 Surface elevations

Surface elevations have been plotted from WAMIT's output using MATLAB. In Fig. 2.11 incident waves come from the left-hand side. Therefore, the left-hand side of the array contains the incident and reflected waves and the right-hand side the transmitted waves.

One may observe, in Fig. 2.11, that for certain angles the reflected wave from the array is quasi-inexistent (e.g. $\theta = 25$ deg and $\theta = 55$ deg). The theory developed by Hu and Chan (2005) can only predict one non-reflection angle, the Brewster angle, because, as mentioned before, that theory only stands for a semi-infinite array of cylinders. This is

why the theory associated with the Fabry-Pérot interferometer has been presented in section 2.3.

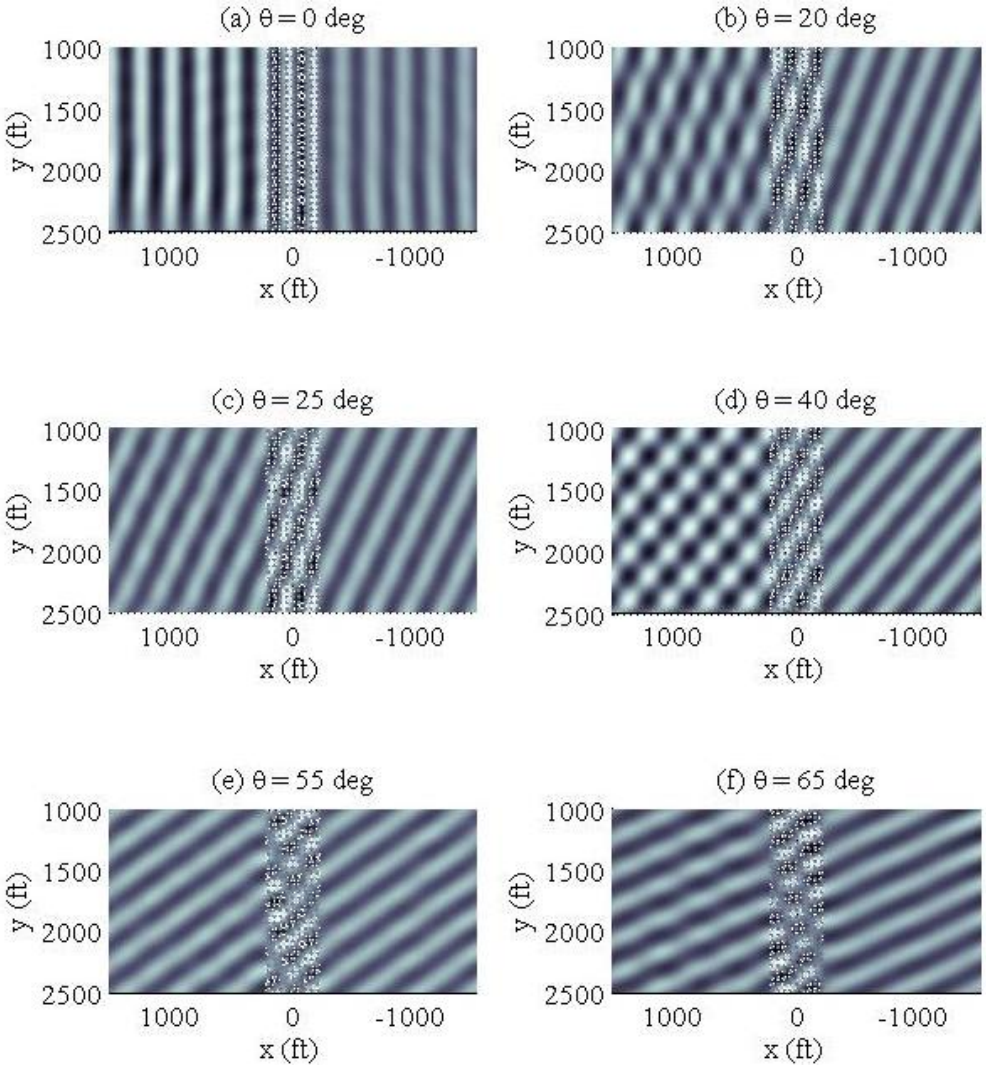

Fig. 2.11. Surface elevations for the incident angles (a) 0 deg, (b) 20 deg, (c) 25 deg, (d) 40 deg, (e) 55 deg and (f) 65 deg. The incident wave comes from the right-hand side.

2.5.2 Validation of the definition of the refractive index

WAMIT has been run for eight different filling ratios and for five different incident angles (0, 20, 40, 60 and 80 deg). For each case, the refractive index has been calculated from WAMIT's surface elevation output by two different ways and for the five incident angles. The first way is to determine the refractive angle inside the array and use Snell's law to calculate the refractive index. The second way is to determine the wavenumber inside the array and use the relation $k_e = n_e\, k$ to find the refractive index.

Refractive indexes calculated with these two methods are very close to the ones determined using expression (2.35) from Hu and Chan, thus validating the theoretical formulation of the refractive index.

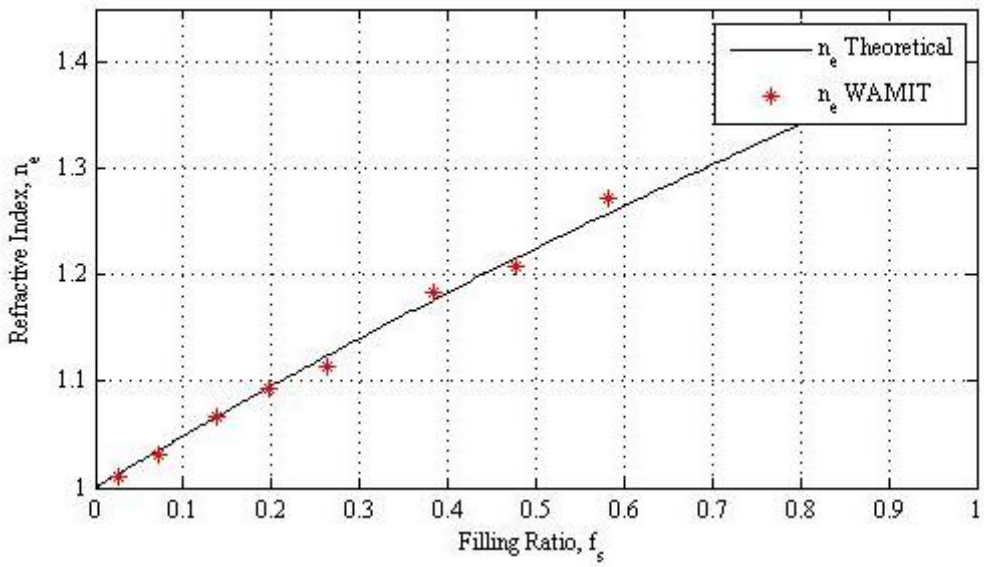

Fig. 2.12. Refractive index n_e as a function of the filling ratio f_s of the array from both theoretical formulation and WAMIT's results.

2.5.3 Refraction coefficients and effective width

Once the definition of the refractive index is verified with WAMIT, the next step is to determine the reflection coefficients for the array using WAMIT output. The surface elevation output from WAMIT are studied and the Maximum Likelihood Method described in section 2.4 is applied to determine the reflection and transmission coefficients. The nine-layer array has been run for twenty different angles (from 0 to 85 degrees) and for six different wave periods (5 sec, 7.99 sec, 8.5 sec, 9.5 sec, 11 sec and 14 sec) with their corresponding wavelengths (124 ft, 250 ft, 270 ft, 310 ft, 368 ft and 481 ft).

The first case has a wave period of T = 5 sec. Results in Fig. 2.13 show that WAMIT's reflection coefficients do not agree with those from the Fabry-Pérot theory described in section 2.3. This could have been predicted: since the wavenumber is equal to k = 0.0508 ft^{-1}, the shallow water condition $kh \ll 1$ is not satisfied ($kh = 2$).

The second run (Fig. 2.14) is the case studied by Hu and Chan which is for a period of T = 7.99 sec. For this case, WAMIT results seem to match the Fabry-Pérot interferometer theory. However, for small incident angles (0 to 30 degrees), some inconsistencies were observed in the results and the curve of WAMIT's reflection results did not perfectly match the theoretical one. This may be the result of the definition of the effective width of the array which implicitly appears in the reflection coefficient formula (2.53). A width w = 450 ft which corresponds to the width of the medium as defined by Hu and Chan was initially chosen. In order to correct the Fabry-Pérot curve for small incident angles we increased the effective width of the array to 480 ft at 0 degrees. Then

the effective width is assumed to linearly decrease to 450 ft at around 30 degrees. The figure on page 44 represents the effective width of the array as a function of the incident angle.

To verify that empirical definition of the effective width of the array, other cases were run for higher periods (8.5, 9.5, 11 and 14 sec). For wave periods of 8.5 sec (Fig. 2.15) and 9.5 sec (Fig. 2.16) the effective width has respectively been corrected to 460 ft and 455 ft at 0 deg. For wave periods of 11 sec (Fig. 2.17) and 14 sec (Fig. 2.18), the effective width does not need to be corrected. Curves obtain for the effective width as depicted in Fig. 2.19 seem to indicate consistency in the empirical definition of the effective width of the array.

Moreover, results from both WAMIT and Fabry-Pérot interferometer lead to non-reflection for certain incident angles. Two effects may explain that phenomenon. The first is the Brewster angle which is due to the non-reflection at one edge of the array. The formulation of the Brewster angle θ_0 given by equation (2.42) leads to $\theta_0 = 72\,\text{deg}$ for the studied array. As expected, Fig. 2.13 through Fig. 2.18 all show zero reflection at 72 degrees. The other effect is the Fabry-Pérot effect and zero-reflections are the results of equation (2.49). Note that Fig. 2.14 is the same case as Hu and Chan. They observed only one Fabry-Pérot non-reflection angle while two Fabry-Pérot non-reflection angles may be seen in our case and are predicted by the theory.

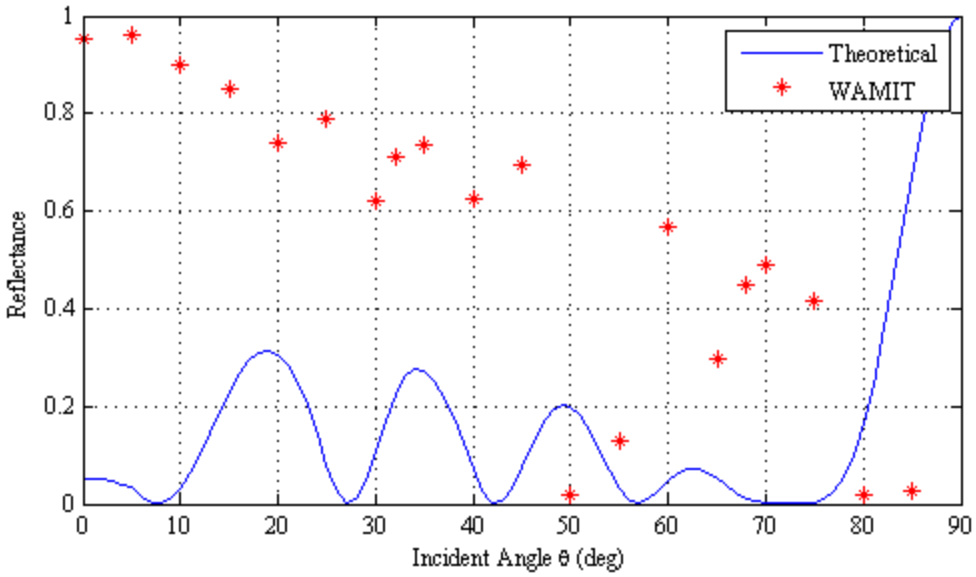

Fig. 2.13. Reflectance from the array of cylinders for an incident wave period T = 5 sec as a function of the incident angle.

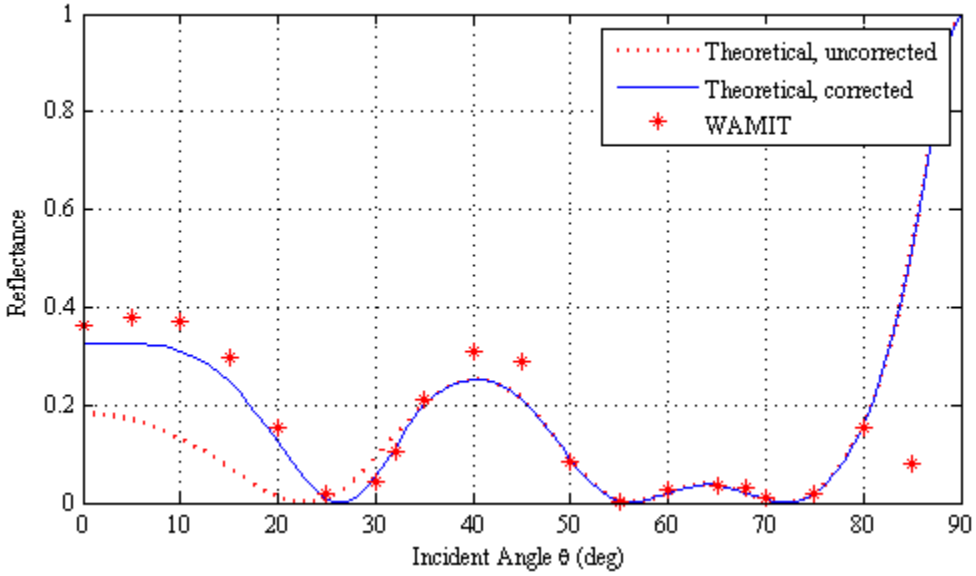

Fig. 2.14. Reflectance from the array of cylinders for an incident wave period T = 7.99sec as a function of the incident angle.

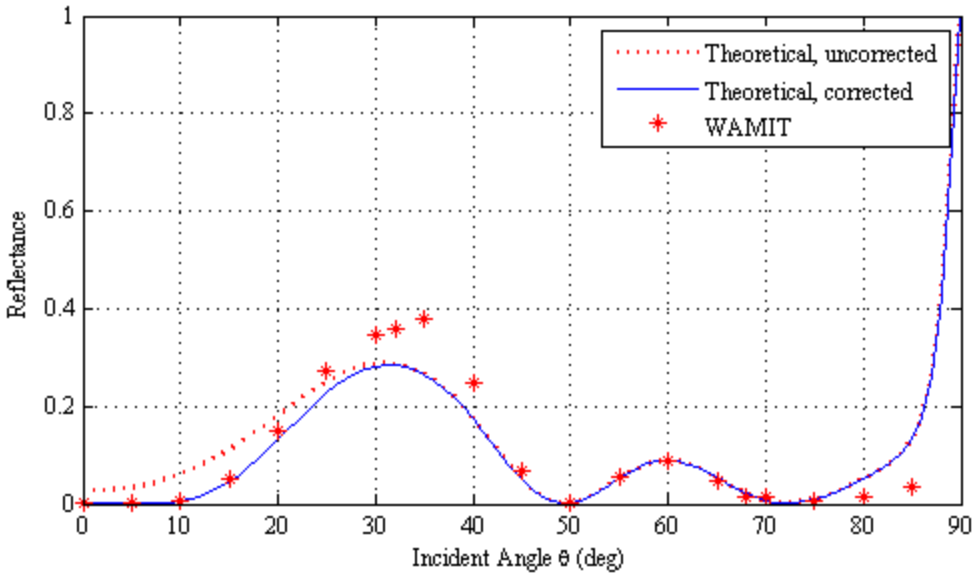

Fig. 2.15. Reflectance from the array of cylinders for an incident wave period T = 8.5 sec as a function of the incident angle.

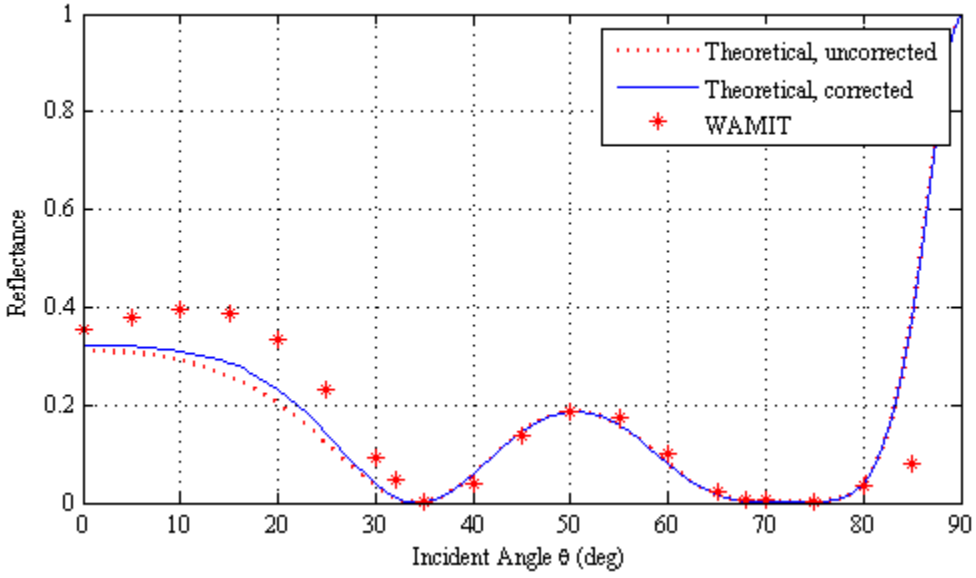

Fig. 2.16. Reflectance from the array of cylinders for an incident wave period T = 9.5 sec as a function of the incident angle.

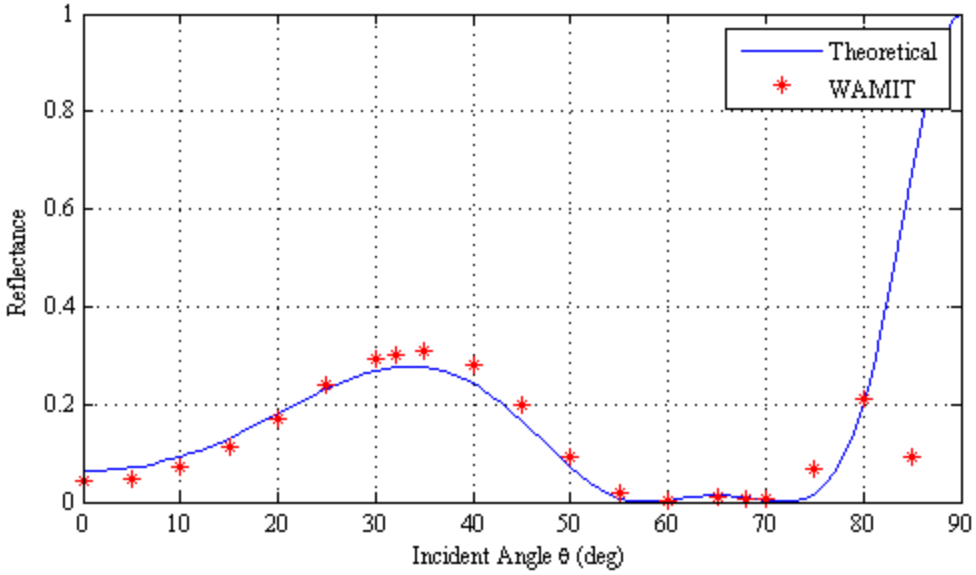

Fig. 2.17. Reflectance from the array of cylinders for an incident wave period T=11 sec as a function of the incident angle.

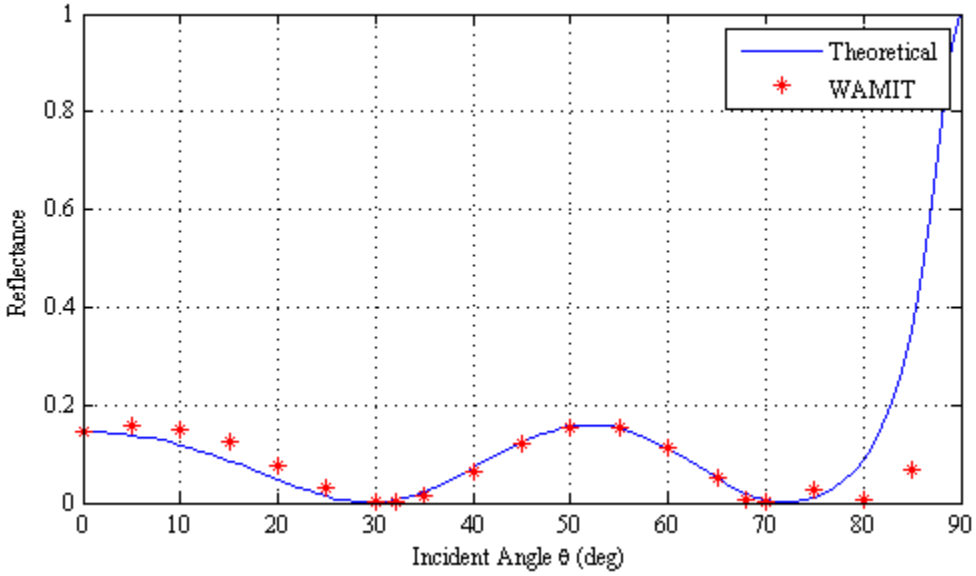

Fig. 2.18. Reflectance from the array of cylinders for an incident wave period T = 14 sec as a function of the incident angle.

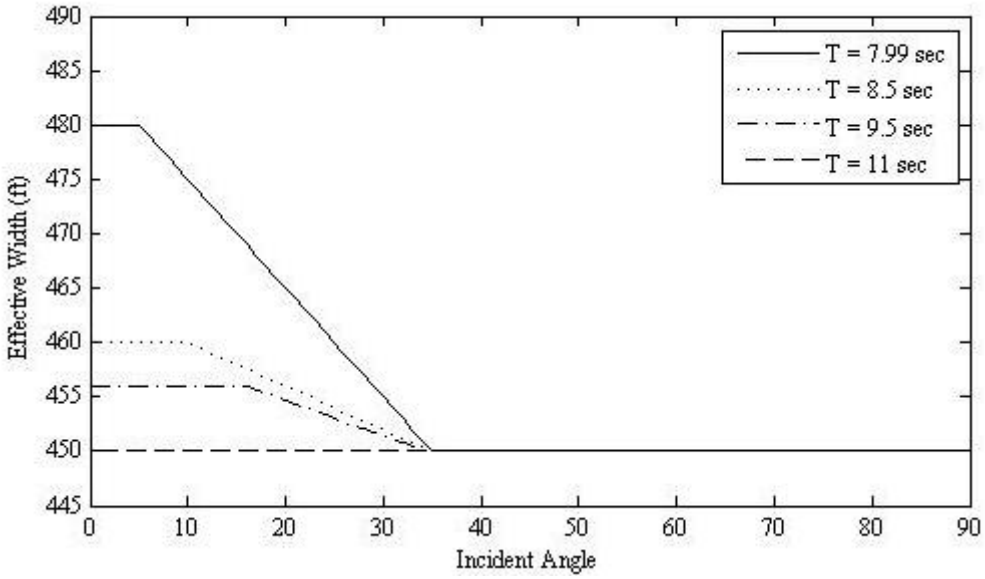

Fig. 2.19. Effective width of the array of cylinders as a function of the incident angle for four different incident wave periods of 7.99 sec, 8.5 sec, 9.5 sec and 11 sec.

2.6 Bi-convex cylinder arrays

Hu and Chan (2005) demonstrated the focusing effect of a bi-convex array of cylinders. This problem is further studied herein in light of the optical analogy. An array of regularly spaced cylinders have been defined to obtain a certain radius of curvature as shown in Fig. 2.20. Planes of symmetry in the X and Y directions have been considered. The first array (case 1) consists in 728 cylinders, it has a radius of curvature of R = 2800 ft and a filling ratio f_s = 0.385 corresponding to a refractive index n_e = 1.17.

Surface elevations (Fig. 2.21, Fig. 2.23 and Fig. 2.25) and wave intensities (Fig. 2.22, Fig. 2.24 and Fig. 2.26) have been plotted with MATLAB.

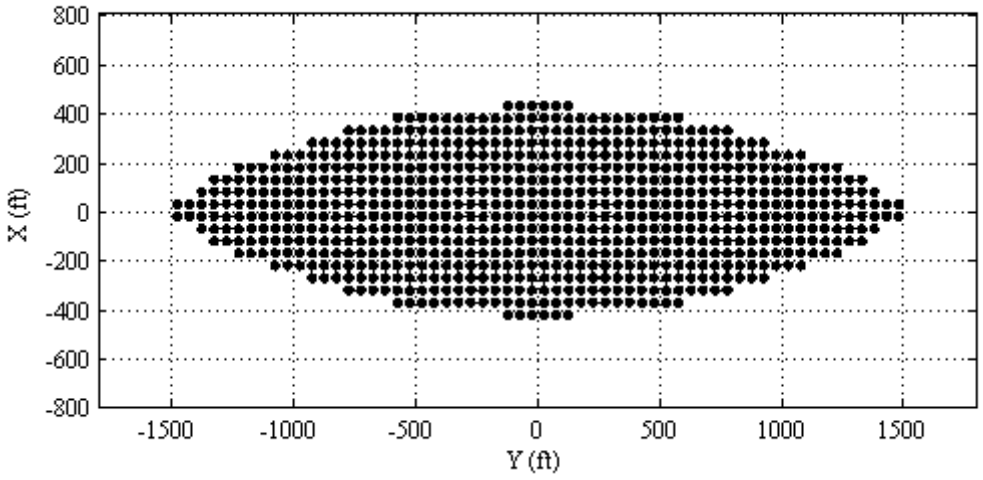

Fig. 2.20. Bi-convex array of 728 cylinders. Coordinates of each cylinder have been inputted in WAMIT.

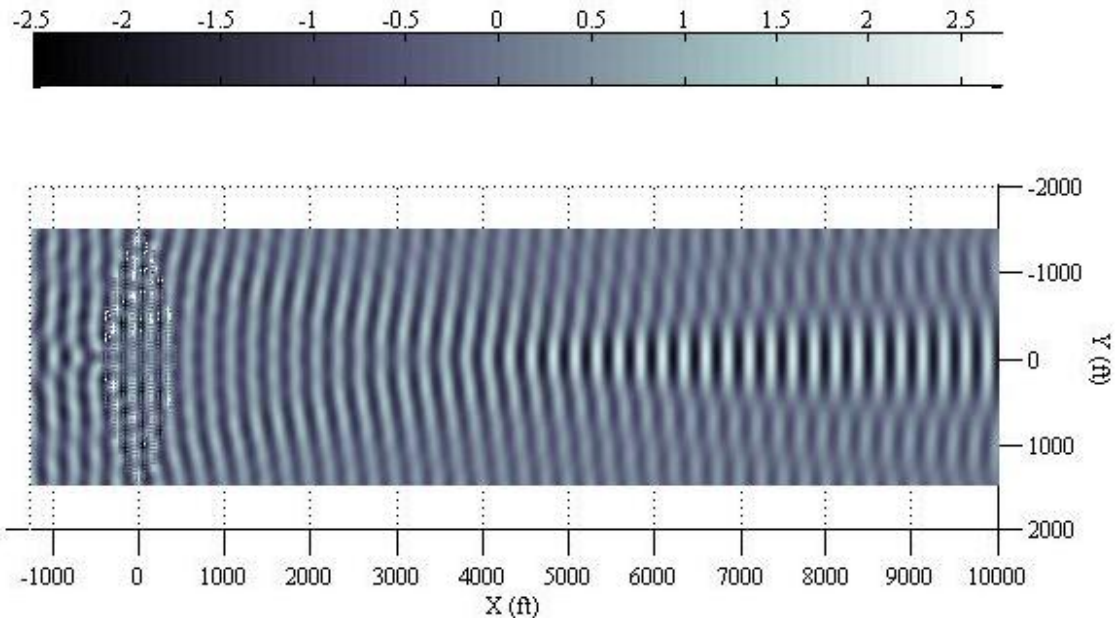

Fig. 2.21. Wave elevation for a bi-convex array of cylinders, for an incident wave period T = 7.99 sec and a filling ratio f_s = 0.385.

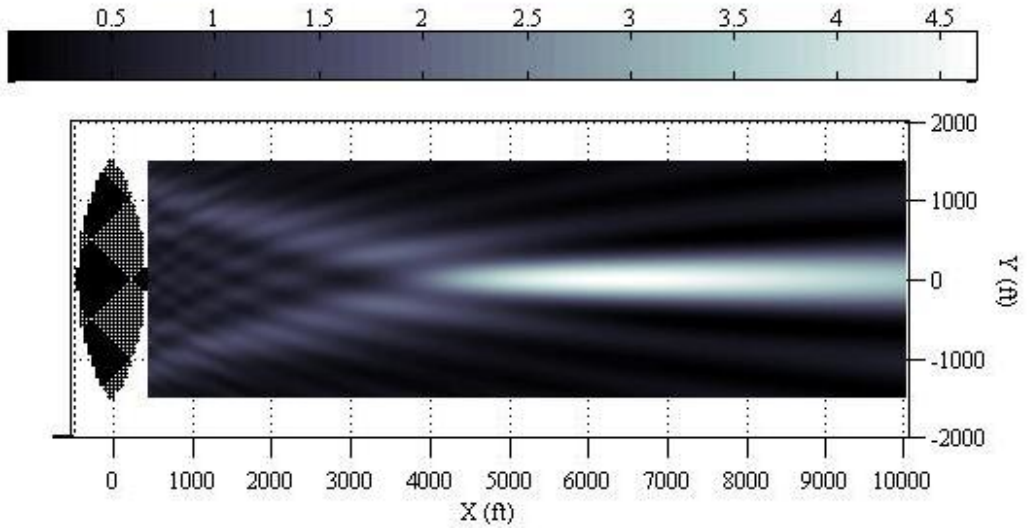

Fig. 2.22. Wave intensity for a bi-convex array of cylinders, for an incident wave period T = 7.99 sec and a filling ratio f_s = 0.385.

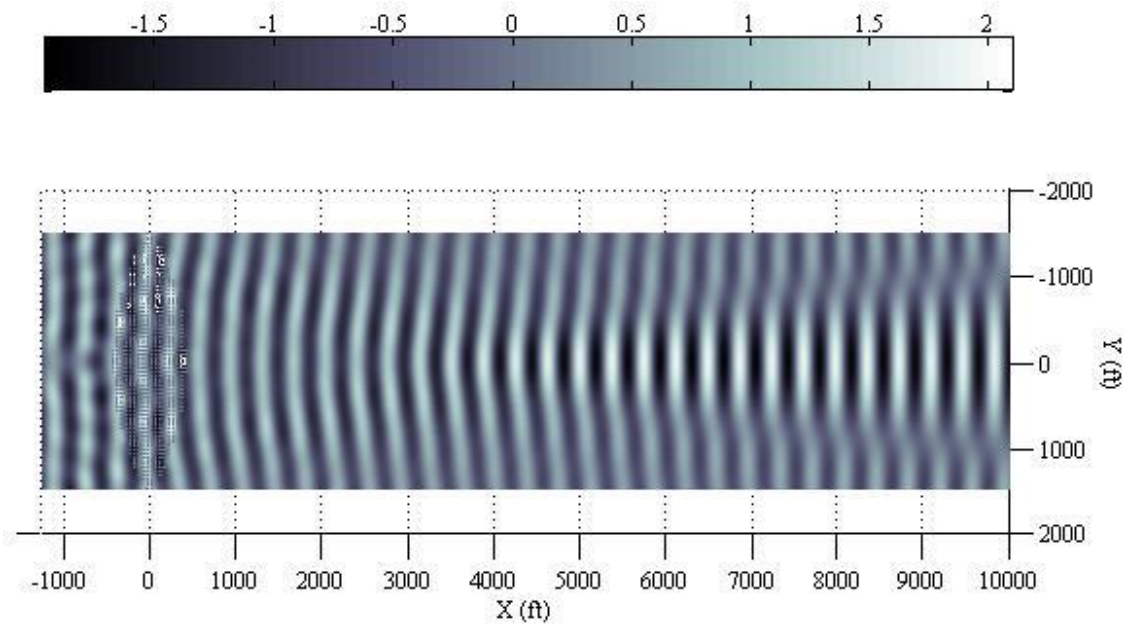

Fig. 2.23. Wave elevation for a bi-convex array of cylinders, for an incident wave period T = 11 sec and a filling ratio f_s = 0.385.

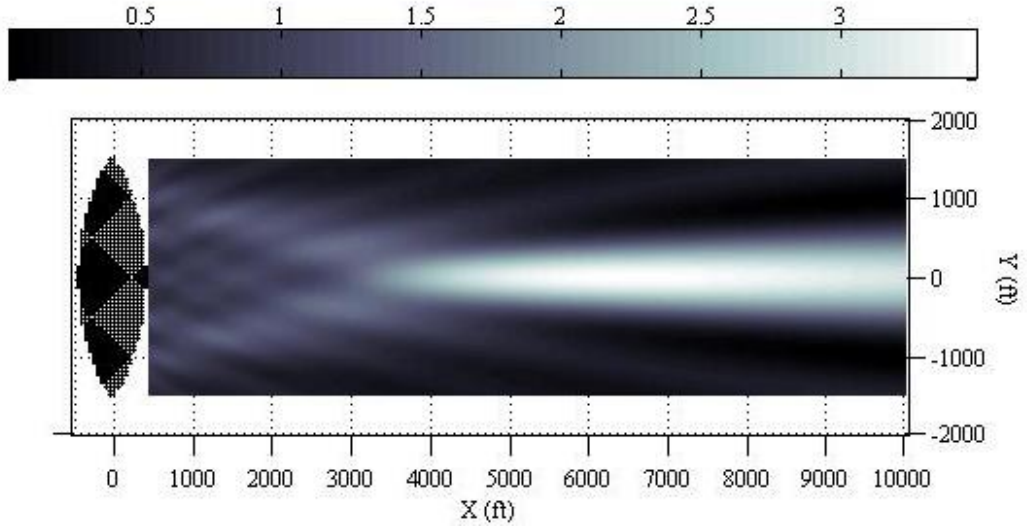

Fig. 2.24. Wave intensity for a bi-convex array of cylinders, for an incident wave period T = 11 sec and a filling ratio f_s = 0.385.

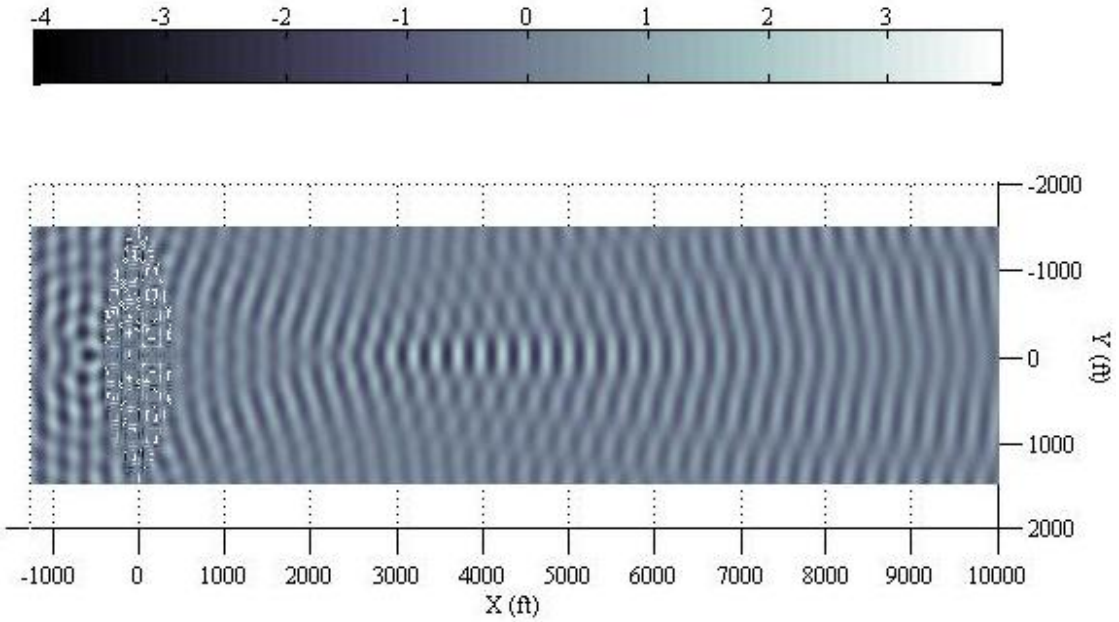

Fig. 2.25. Wave elevation for a bi-convex array of cylinders, for an incident wave period T = 7.99 sec and a filling ratio f_s = 0.581.

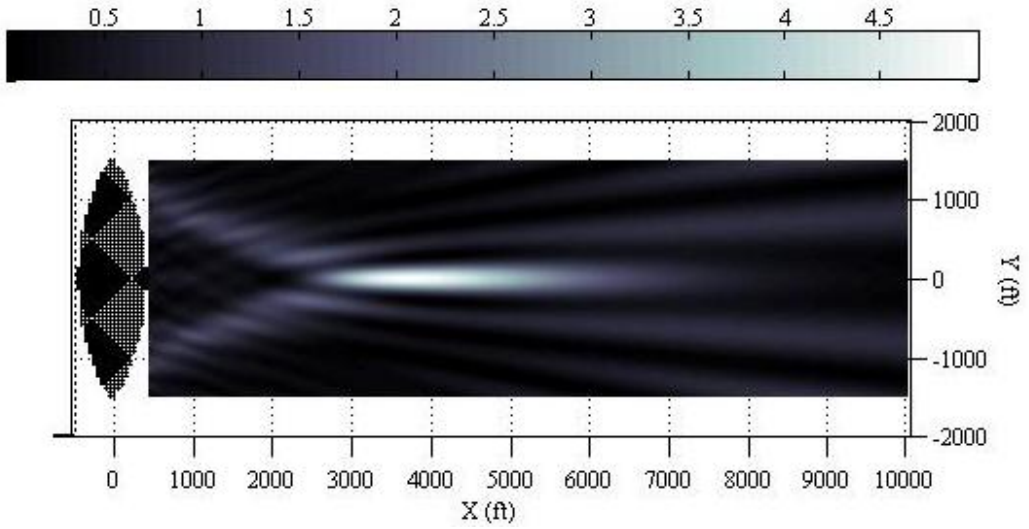

Fig. 2.26. Wave intensity for a bi-convex array of cylinders, for an incident wave period T = 7.99 sec and a filling ratio f_s = 0.581.

Fig. 2.22, Fig. 2.24 and Fig. 2.26 show an area where the wave energy is focused. In order to relate this phenomenon to optical properties, the intensity has been plotted along the X-direction (see Fig. 2.27 and Fig. 2.28). One can observe that a point with maximum intensity exists for the three studied cases.

The first and second cases (case 1 and 2) have the same filling ratio f_s = 0.385 but they have two different wave periods T1 = 7.99 sec and T2 = 11 sec. Fig. 2.27 shows that the maximum intensity is located almost at the same point for both cases. Thus, in a first approach, it may be concluded that the location of the maximum wave intensity does not depend on the wave period. However, Fig. 2.27 also indicates that the maximum wave intensity is higher for short wave periods (e.g. case 1, T1 = 7.99 sec) and decreases for longer wave periods (e.g. case 2, T2 = 11 sec). It is also noted in Fig. 2.28, which represents the wave intensity in the Y-direction at the maximum intensity in the X-direction, that the maximum intensity is more narrow for shorter wave periods.

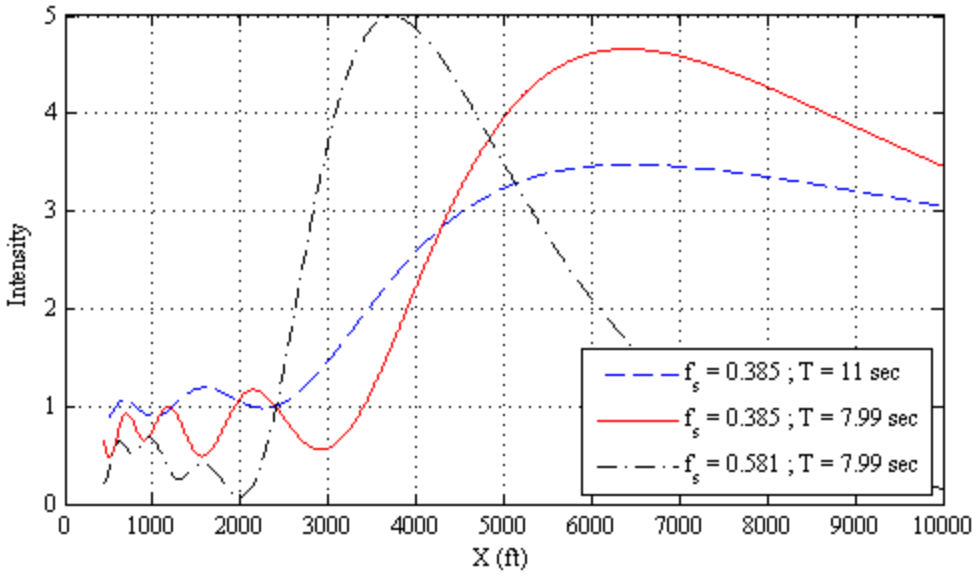

Fig. 2.27. Wave intensity along the X-direction for a bi-convex array of cylinders, for incident wave periods of 7.99 sec and 11 sec and filling ratios of 0.385 and 0.581.

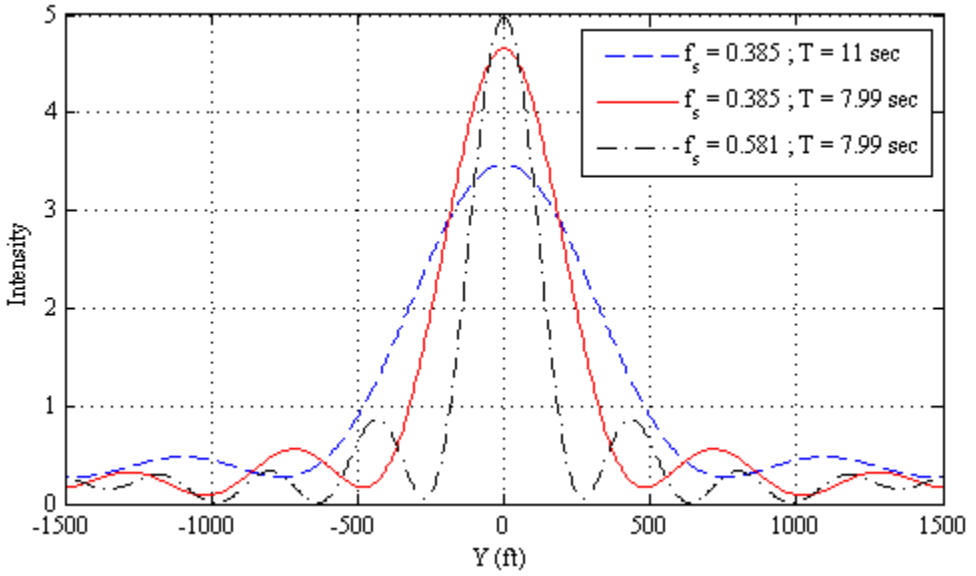

Fig. 2.28. Wave intensity along the Y-direction for a bi-convex array of cylinders, for incident wave periods of 7.99 sec and 11 sec and filling ratios of 0.385 and 0.581.

The third case (case 3) has a filling ratio f_s = 0.581 and a wave period T = 7.99 sec. The maximum wave intensity for this case is observed to be at a location closer to the array than it was for case 1. The filling ratio represents the density of the array.

If optical analogies are considered, an optical converging lens can be studied. In optics, the point where the light is focused is called the focal point and it depends on the density and the curvature of the focusing lens. The following formula of the focal point can be found in the basic optical literature:

$$\frac{1}{f} = (n-1)\left(\frac{1}{R_1} - \frac{1}{R_2}\right)\left(1 + \frac{n-1}{n}\frac{e}{R_2 - R_1}\right) \tag{2.85}$$

where f is the focal distance, n is the index of refraction of the lens, e is the width of the lens, R_1 is the radius of curvature of the first edge of the lens and R_2 is the radius of curvature of the second edge of the lens as shown in Fig. 2.29.

In the studied case, both edges have the same radius of curvature, thus $R_2 = -R_1$.

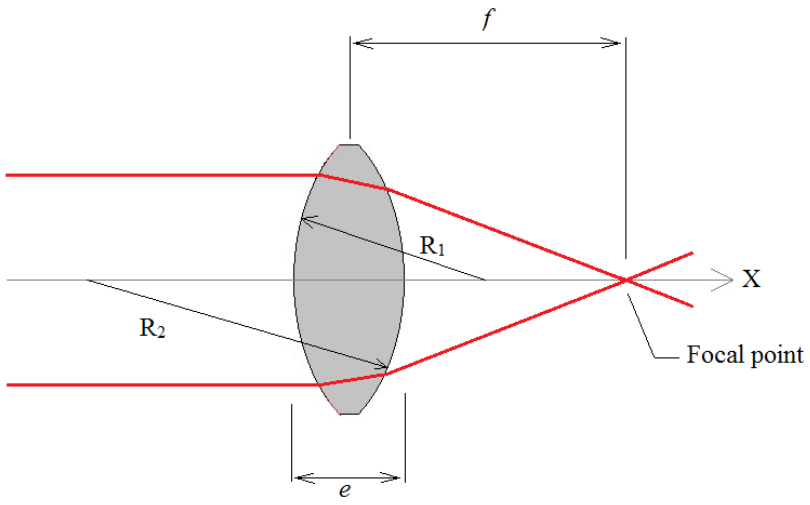

Fig. 2.29. Converging lens.

Equation (2.85) indicates that the focal distance basically depends on the radius of curvature, the width of the lens and the index of refraction of the lens. In Fig. 2.30, theoretical curves for the focal distance are plotted as functions of the curvature and the index of refraction. The two plotted points correspond to the maximum of wave intensity for case 1 and case 3. The maximum of intensity is then related to the focal distance.

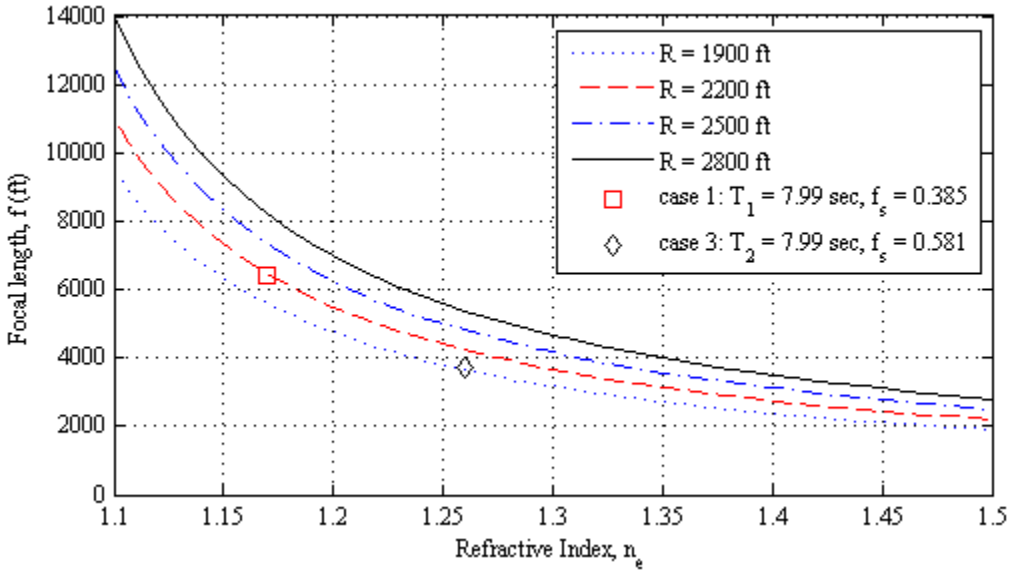

Fig. 2.30. Focal distance as a function of the refractive index n_e and the radius of curvature R. Focal distances for both case 1 and case 3 are represented respectively by a square and a diamond.

Case 1 and 3 corresponds to a radius of curvature R = 2800 ft. However, one can observe in Fig. 2.30 that the effective radius of curvature of the array is between 1900 ft and 2200 ft.

In section 2.5.3, the effective width has been discussed for a rectangular array of rigid cylinders. It was observed that for small incident angles (below 30 degrees), the width of the array has to be corrected and the resulting effective width is larger than the

real width. If the same principle is applied in the present case, it can be shown that the effective radius of curvature of the bi-convex array is smaller than the real radius of curvature. In fact, as shown in Fig. 2.31, the incident wave has an incident angle close to 0 degree at the center of the array which leads to a larger width of the array and thus to a smaller radius of curvature. The incident angle increases for incident waves at both edges of the array.

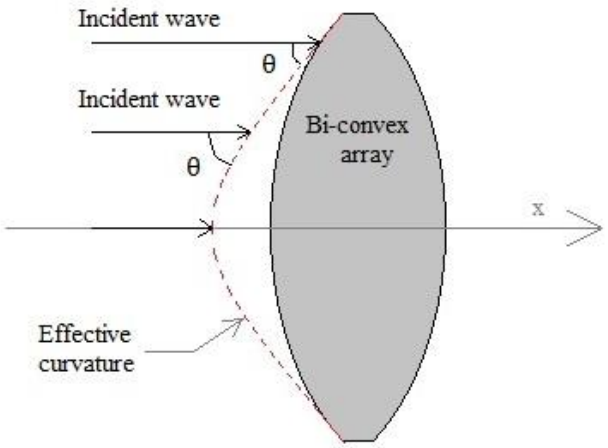

Fig. 2.31. Effective curvature of a bi-convex array of cylinders.

It was also seen that the effective width has to be increased for small wave periods in the rigid array case. In the lens case, the location of the focal point does not depend on the wave period. Thus, other unknown phenomena are needed to explain the difference between the focal length predicted by optical theory and WAMIT results.

3. ARRAYS OF ELASTIC CYLINDERS

The study of wave diffraction by regular arrays of rigid cylinders was used to verify the set up of the WAMIT model for a subsequent study of wave attenuation by arrays of elastic cylinders. As explained in the introduction, the motivation is to study similar behaviors that occur in the acoustical problem presented by Junger and Cole (1980). In fact, Junger and Cole studied sound propagation in a bubble swarm and found that sound attenuation is more effective when the sound frequency is in the range of the natural pulsating frequencies of the bubbles.

In this section, bubbles are replaced by flexible/elastic cylinders which can have circumferential deformations. These deformations are decomposed in a set of modes. the first one is a "breathing" mode and has a similar behavior as a pulsating bubble. The theory for the equations of motion, the natural frequency of the cylinders and the mass and stiffness matrices, which will be implemented in WAMIT, are first presented in this section. WAMIT results are then discussed for the case of a single cylinder.

3.1 Theoretical background

3.1.1 Displacements

The system considered is a closed circular cylindrical shell of length L clamped at the bottom and at the top. Therefore, radial displacements are impossible at the top and bottom. A thin shell is a body bounded by two curved surfaces. The distance between these two surfaces is small compared to the other dimensions of the shell (radius and length).

Because of the geometry of the body, cylindrical coordinates are used to describe the evolution of the system. The cylinder is no longer rigid but elastic and the surface of the body has displacements of the form:

$$u_n(\mathrm{z},\theta) = \alpha_n \cos\lambda z \cos n\theta \tag{3.1}$$

$$v_n(\mathrm{z},\theta) = \beta_n \sin\lambda z \sin n\theta \tag{3.2}$$

$$w_n(\mathrm{z},\theta) = \gamma_n \sin\lambda z \cos n\theta \tag{3.3}$$

where u_n, v_n and w_n are respectively the displacements in vertical, tangential and radial directions as shown in Fig. 3.1 and $\alpha_n, \beta_n, \gamma_n$ are the corresponding amplitudes for these displacements.

Hence, the total displacements U, V and W of the body may be expanded into a Fourier series in θ:

$$U(\mathrm{z},\theta) = \sum_{n=0}^{\infty} \alpha_n \cos\lambda z \cos n\theta \tag{3.4}$$

$$V(\mathrm{z},\theta) = \sum_{n=0}^{\infty} \beta_n \sin \lambda z \sin n\theta \tag{3.5}$$

$$W(\mathrm{z},\theta) = \sum_{n=0}^{\infty} \gamma_n \sin \lambda z \cos n\theta \tag{3.6}$$

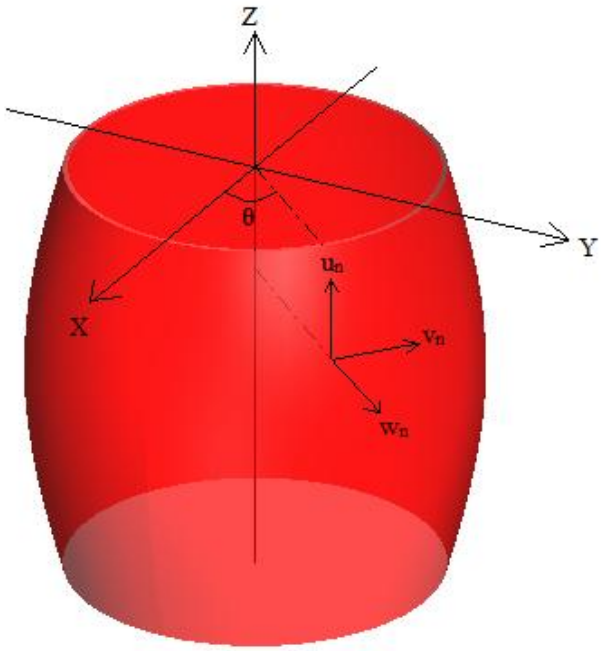

Fig. 3.1. Cylindrical coordinates and displacements.

To satisfy the boundary condition (v = w = 0 at z = 0 and z = L) the parameter λ may be set as:

$$\lambda = \frac{\pi}{L} \tag{3.7}$$

The presence of $\sin \lambda z$ in the equations (3.2) and (3.3) implies no displacement at the bottom and top of the cylinder and a maximum displacement at mid-depth which

corresponds to a cylinder clamped at both top and bottom. Radial displacements are represented in Fig. 3.2. The effect of setting $\lambda = \frac{\pi}{L}$ is visible in Fig. 3.3 where the first four displacements are represented in 3D.

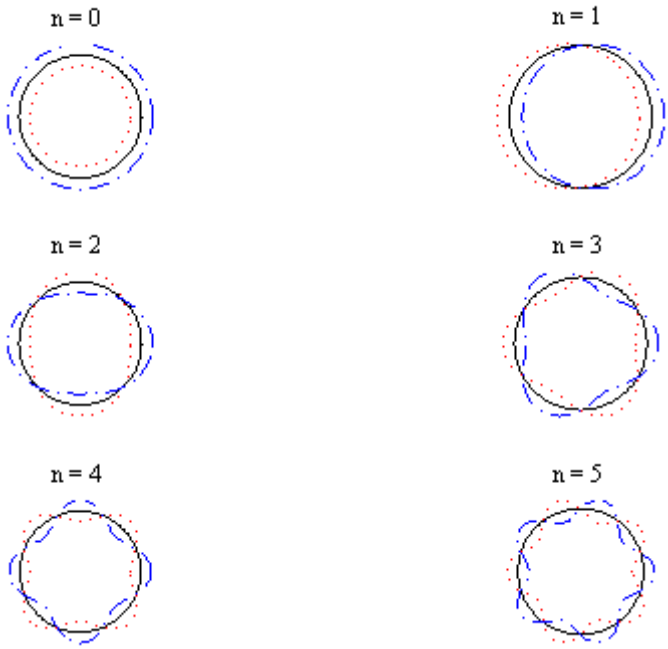

Fig. 3.2. First six circumferential displacement modes at z = L/2.

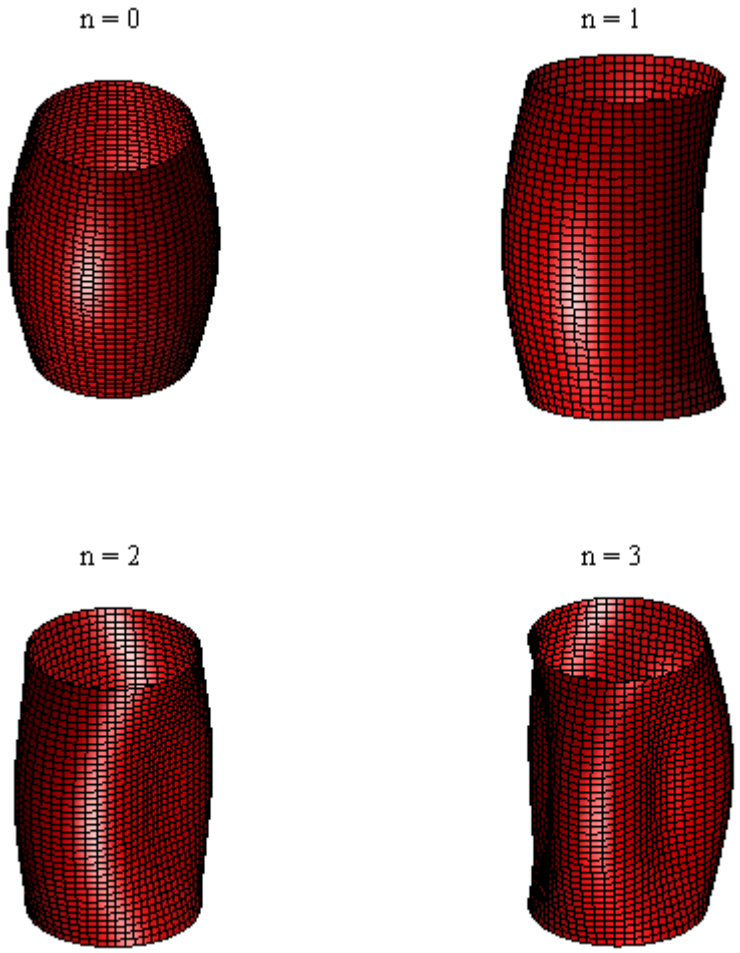

Fig. 3.3. First four circumferential displacement modes in 3D.

A clamped cylinder at both bottom and top is physically realistic, Fig. 3.4 gives an example for the structure of such a cylinder. It is constituted of two rigid circular frames linked by a rigid vertical rod. This assembly serves as a backbone for the elastic vertical shell that is wrapped around and clamped to the top and the bottom frames.

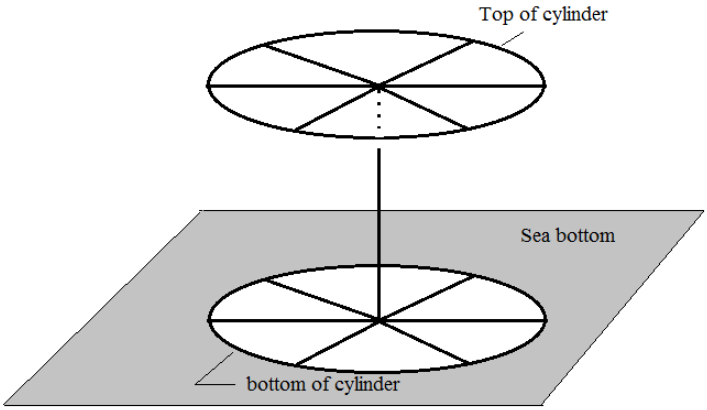

Fig. 3.4. Example of a structure for a bottom-mounted cylinder which is clamped at the bottom and at the top.

The displacement mode corresponding to $n = 0$ is called the "breathing" mode and its natural frequency will receive particular attention, especially in choosing the material properties of the cylindrical shell.

3.1.2 Diffraction and radiation potentials

As for the single rigid cylinder, the incident wave can be expressed as:

$$\phi_I = -i\frac{gA}{\omega}\frac{\cosh(k(z+h))}{\cosh(kh)}\left\{\sum_{n=0}^{\infty}\varepsilon_n J_n(kr)\cos(n\theta)\right\}e^{-i\omega t} \tag{3.8}$$

and the solution for the first-order scattered wave is given by MacCamy and Fuchs:

$$\phi_s = i\frac{gA}{\omega}\frac{\cosh(k(z+h))}{\cosh(kh)}\left\{\sum_{n=0}^{\infty}\varepsilon_n \frac{J_n'(kR)}{H_n'(kR)} H_n(kr)\cos(n\theta)\right\}e^{-i\omega t} \tag{3.9}$$

In fact, for the deformable cylinder, the scattering potential is the same as the one for the non-deformable body as specified by Newman (1994).

Dean and Dalrymple (1991) presented an analytical solution for the radiation potential of a cylindrical wavemaker which has radial displacements. This solution has been modified in order to account for the zero-displacement at the top and at the bottom of the cylinder. The resulting expression is then used to formulate the radiation potential of the cylindrical shell.

The total radiation potential due to the body's motions can be written as a linear combination of the radiation potential due to each mode of displacement:

$$\phi_R = \sum_{n=0}^{N}\xi_n\phi_{R,n} \tag{3.10}$$

where ξ_n is the amplitude of the displacement corresponding to the n-th mode

$$\xi_n = \begin{bmatrix}\alpha_n & 0 & 0\\ 0 & \beta_n & 0\\ 0 & 0 & \gamma_n\end{bmatrix} \tag{3.11}$$

and $\phi_{R,n}$ is the radiation potential due to the n-th mode with:

$$\phi_{R,n} = \begin{bmatrix} 0 \\ 0 \\ \phi_{R\gamma,n} \end{bmatrix} \tag{3.12}$$

$$\phi_{R\gamma,n} = A_p H_n^{(1)}(k_p r)\cosh[k_p(h+z)]\{\cos(n\theta)e^{i\omega t}\} + \sum_{m=1}^{\infty} C_m K_n(k_m r)\cos[k_m(h+z)]\{\cos(n\theta)e^{i\omega t}\} \tag{3.13}$$

The first term corresponds to the propagating mode while the second term corresponds to the evanescent modes.

The wavenumbers k_p and k_m are calculated using the following dispersion relations:

$$\omega^2 = g k_p \tanh(k_p h) \tag{3.14}$$

$$\omega^2 = -g k_m \tan(k_m h) \tag{3.15}$$

Equation (3.14) is the dispersion relationship for progressive waves and k_p is real. The second relationship (3.15) gives the wavenumbers for standing waves which have amplitudes that decrease exponentially with distance from the cylinder.

Coefficients A_p and C_m are determined by the lateral boundary conditions at the cylinder:

$$A_p = \frac{\int_{-h}^{0} \sin(\lambda z)\cosh[k_p(h+z)]dz}{k_p\left[H_n^{(1)}(k_p a)\right]' \int_{-h}^{0} \cosh^2[k_p(h+z)]dz} \tag{3.16}$$

$$C_m = \frac{\int_{-h}^{0} \sin(\lambda z)\cos[k_m(h+z)]dz}{k_m\left[H_n^{(1)}(k_m a)\right]' \int_{-h}^{0} \cos^2[k_m(h+z)]dz} \tag{3.17}$$

A kinematic boundary condition has been applied to the moving surface of the cylinder to obtain equation (3.13) and its associated coefficients A_p and C_m. It accounts for the

radial displacement of the surface and the fact that the cylinder is clamped at the top and bottom. The linear kinematic condition is:

$$-\frac{\partial \phi_{R,n}}{\partial r} = \frac{\sin(\lambda z)}{2}\,\omega\cos(\omega t) \tag{3.18}$$

In this research, equation (3.13) is used to validate the solution given by WAMIT for the radial potential due to the first order "breathing" displacement.

Finally, the total velocity potential ϕ can be expressed by:

$$\phi = \phi_D + \phi_R \tag{3.19}$$

3.1.3 Equations of motion

The theory of the vibration of thin shells from Leissa (1973) is used to describe the motion of the elastic cylinder. The equations of motion are derived using the theory of surfaces. In fact the deformation of the shell is determined by the displacement of the surface. In the present case, the equations of Donnell and Mushtari have been used. They come from the standard derivation using Love's first approximation. For this approximation the following assumptions must be considered (Leissa 1973):

- *The thickness of the shell is small compared to other dimensions of the body.*

- *Strains and displacement are small enough to neglect second order in the strain displacement relations.*

- *The transverse normal stress is small compared with the other normal stress components and may be neglected.*

- *Normals to the underformed middle surface remain straight and normal to the deformed middle surface and suffer no extension*.

According to the Donnell-Mushtari theory for vibrations of thin cylindrical shells, the equations of motion can be written as:

$$[\mathcal{L}]\{u_i\} = \{0\} \tag{3.20}$$

with

$$\{u_i\} = \begin{bmatrix} u_i \\ v_i \\ w_i \end{bmatrix} \tag{3.21}$$

where $\{u_i\}$ is the displacement vector and u_i, v_i and w_i are respectively the displacements in the vertical, tangential and radial directions. $[\mathcal{L}]$ is a 3-by-3 matrix:

$$[\mathcal{L}] = \begin{bmatrix} a_{11} & a_{12} & a_{13} \\ a_{21} & a_{22} & a_{23} \\ a_{31} & a_{32} & a_{33} \end{bmatrix} \tag{3.22}$$

with

$$a_{11} = \frac{\partial^2}{\partial z^2} + \frac{(1-\nu)}{2}\frac{\partial^2}{\partial \theta^2} - \rho\frac{(1-\nu^2)R^2}{E}\frac{\partial^2}{\partial t^2} \tag{3.23}$$

$$a_{12} = a_{21} = \frac{(1+\nu)}{2}\frac{\partial^2}{\partial z \partial \theta} \tag{3.24}$$

$$a_{13} = \nu\frac{\partial}{\partial z} \tag{3.25}$$

$$a_{22} = \frac{(1-\nu)}{2}\frac{\partial^2}{\partial z^2} + \frac{\partial^2}{\partial \theta^2} - \rho\frac{(1-\nu^2)R^2}{E}\frac{\partial^2}{\partial t^2} \tag{3.26}$$

$$a_{23} = a_{32} = \frac{\partial}{\partial \theta} \tag{3.27}$$

$$a_{33} = 1 + k\nabla^4 + \rho\frac{(1-\nu^2)R^2}{E}\frac{\partial^2}{\partial t^2} \tag{3.28}$$

In these equations, ν is the Poisson's coefficient, E the Young's modulus, ρ the density of the material and $k = \frac{h^2}{12R^2} \ll 1$.

Substituting u_i, v_i and w_i by relations (3.1), (3.2) and (3.3), the equations of motion become

$$[\mathcal{L}'] \begin{bmatrix} \alpha_n \\ \beta_n \\ \gamma_n \end{bmatrix} = \{0\} \tag{3.29}$$

with

$$[\mathcal{L}'] = \begin{bmatrix} a_{11}{}' & a_{12}{}' & a_{13}{}' \\ a_{21}{}' & a_{22}{}' & a_{23}{}' \\ a_{31}{}' & a_{32}{}' & a_{33}{}' \end{bmatrix} \tag{3.30}$$

and

$$a_{11}{}' = -\lambda^2 - \frac{1-\nu}{2} n^2 + \frac{\rho(1-\nu^2)R^2\omega^2}{E} \tag{3.31}$$

$$a_{12}{}' = a_{21}{}' = \frac{1+\nu}{2} \lambda n \tag{3.32}$$

$$a_{13}{}' = -a_{31}{}' = \nu\lambda \tag{3.33}$$

$$a_{22}{}' = -\frac{1-\nu}{2} \lambda^2 - n^2 + \frac{\rho(1-\nu^2)R^2\omega^2}{E} \tag{3.34}$$

$$a_{23}{}' = -a_{32}{}' = -n \tag{3.35}$$

$$a_{33}{}' = 1 + k(\lambda^2 + n^2)^2 - \frac{\rho(1-\nu^2)R^2\omega^2}{E} \tag{3.36}$$

3.1.4 Mass and stiffness matrices

The mass and stiffness matrices for the cylindrical shell can be defined following Newman's procedure (1994).

In fact the operator $[\mathcal{L}']$ in equation (3.30) can be rewritten as

$$[\mathcal{L}'] = \frac{(1-\nu^2)\mathrm{R}}{\mathrm{E}}([\mathcal{L}_s] - \omega^2[\mathcal{L}_m]) \tag{3.37}$$

where

$$[\mathcal{L}_s] = \begin{bmatrix} b_{11} & b_{12} & b_{13} \\ b_{21} & b_{22} & b_{23} \\ b_{31} & b_{32} & b_{33} \end{bmatrix} \tag{3.38}$$

and

$$[\mathcal{L}_m] = \rho R \begin{bmatrix} 1 & 0 & 0 \\ 0 & 1 & 0 \\ 0 & 0 & 1 \end{bmatrix} \tag{3.39}$$

with

$$b_{11} = \frac{\mathrm{E}}{(1-\nu^2)\mathrm{R}}\left[-\lambda^2 - \frac{1-\nu}{2}n^2\right] \tag{3.40}$$

$$b_{12} = b_{21} = \frac{\mathrm{E}}{(1-\nu^2)\mathrm{R}}\left[\frac{1+\nu}{2}\lambda n\right] \tag{3.41}$$

$$b_{13} = -b_{31} = \frac{\mathrm{E}}{(1-\nu^2)\mathrm{R}}[\nu\lambda] \tag{3.42}$$

$$b_{22} = \frac{\mathrm{E}}{(1-\nu^2)\mathrm{R}}\left[-\frac{1-\nu}{2}\lambda^2 - n^2\right] \tag{3.43}$$

$$b_{23} = -b_{32} = \frac{\mathrm{E}}{(1-\nu^2)\mathrm{R}}[-n] \tag{3.44}$$

$$b_{33} = \frac{\mathrm{E}}{(1-\nu^2)\mathrm{R}}[1 + k(\lambda^2 + n^2)^2] \tag{3.45}$$

Hence, the equation (3.29) becomes

$$([\mathcal{L}_s] - \omega^2[\mathcal{L}_m])\{\xi_n\} = F \tag{3.46}$$

where F is the first order pressure force.

Besides, the displacement can be decomposed in a set of modes f_n (n = 0,...,N):

$$\xi(z,\theta) = \sum_n \xi_n f_n(z,\theta) \tag{3.47}$$

where

$$f_n(z,\theta) = \begin{bmatrix} \cos(\lambda z)\cos(n\theta) \\ \sin(\lambda z)\sin(n\theta) \\ \sin(\lambda z)\cos(n\theta) \end{bmatrix} \tag{3.48}$$

Substituting (3.47) into (3.46) and using the method of weighted residuals (equation (3.46) is multiplied by $\{f_i(z,\theta)\}^T$ and integrated over depth and contour):

$$\begin{aligned} \sum_j \xi_j \int_{-h}^{0}\int_{0}^{2\pi} \{f_i(z,\theta)\}^T([\mathcal{L}_s] - \omega^2[\mathcal{L}_m])\{f_j(z,\theta)\}\,\mathrm{d}\theta\,\mathrm{d}z \\ = \int_{-h}^{0}\int_{0}^{2\pi} \{f_i(z,\theta)\}^T \mathrm{F}(\mathrm{z},\theta)\,\mathrm{d}\theta\,\mathrm{d}z \end{aligned} \tag{3.49}$$

which can be rewritten as

$$\sum_j \xi_j\left(-\omega^2 M_{ij} + C_{ij}\right) = \int_{-h}^{0}\int_{0}^{2\pi} \{f_i(z,\theta)\}^T \mathrm{F}(\mathrm{z},\theta)\,\mathrm{d}\theta\,\mathrm{d}z \tag{3.50}$$

with

$$M_{ij} = \int_{-h}^{0}\int_{0}^{2\pi} \{f_i(z,\theta)\}^T[\mathcal{L}_s]\{f_j(z,\theta)\}\,\mathrm{d}\theta\,\mathrm{d}z \tag{3.51}$$

$$C_{ij} = \int_{-h}^{0} \int_{0}^{2\pi} \{f_i(z,\theta)\}^T [\mathcal{L}_m] \{f_j(z,\theta)\} \, \mathrm{d}\theta \, \mathrm{d}z \tag{3.52}$$

where M_{ij} is the mass matrix and C_{ij} is the stiffness matrix.

3.1.5 Added-mass, damping and wave-exciting forces

Added-mass a_{ij} and damping coefficients b_{ij}, generalized wave-exiting force X_i, and hydrostatic coefficients c_{ij} are evaluated by WAMIT. Their analytical formulations are given by Newman (1994).

The first order-pressure force F can be decomposed on the set of modes and the resulting form is:

$$F_i = \iint_{S_b} p n_i dS = -\rho \iint_{S_b} (i\omega\phi + \mathrm{gz}) n_i dS \tag{3.53}$$

where p is the fluid pressure from the Bernoulli equation.

The right-hand side of equation (3.53) includes the contribution of diffraction and radiation potentials to the first-order pressure force F. If the terms corresponding to the radiation potential are moved to the left side of equation (3.50), the following conventional equations of motion are obtained:

$$\sum_j \xi_j \left(-\omega^2 \left(M_{ij} + a_{ij}\right) + i\omega b_{ij} + C_{ij} + c_{ij}\right) = X_i \tag{3.54}$$

3.1.6 Natural frequency

The natural frequency of the elastic cylinder may be evaluated by calculating the determinant of $[\mathcal{L}']$.

Denoting

$$\Omega^2 = \frac{\rho(1-\nu^2)R^2\omega^2}{E} \tag{3.55}$$

the determinant of $[\mathcal{L}']$ leads therefore to

$$\Omega^6 - K_2\Omega^4 + K_1\Omega^2 - K_0 = 0 \tag{3.56}$$

where

$$K_2 = 1 + \frac{1}{2}(3-\nu)(n^2+\lambda^2) + k(n^2+\lambda^2)^2 \tag{3.57}$$

$$K_1 = \frac{1}{2}(1-\nu)\left[(3+2\nu)\lambda^2 + n^2 + (n^2+\lambda^2)^2 + \frac{(3-\nu)}{(1-\nu)}k(n^2+\lambda^2)^3\right] \tag{3.58}$$

$$K_0 = \frac{1}{2}(1-\nu)[(1-\nu^2)\lambda^4 + k(n^2+\lambda^2)^4] \tag{3.59}$$

The equation (3.56) has three roots. According to Leissa (1973), the larger one corresponds to radiation displacements.

Then material properties are chosen so that the natural period of the shell is in the range of the studied wave frequencies.

3.2 Single elastic cylinder: WAMIT's results

3.2.1 Circumferential modes in WAMIT

As explained in the introduction, deformation modes have been incorporated in WAMIT's subroutine NEWMODES. These modes were defined in cylindrical coordinates in section 3.1 but the geometry of the body has to be specified in Cartesian coordinates in WAMIT. Thus, modes in section 3.1 have been projected on the Cartesian coordinates. Furthermore, for this problem the fluid pressures induced by the tangential modes may be neglected compared to those induced by the radial modes.

Circumferential modes are now defined by:

$$u_{x,n}(x,y,z) = \sin\left(\pi\frac{z}{h}\right)\cos\left(n\,\mathrm{acos}\left(\frac{x}{\sqrt{x^2+y^2}}\right)\right)\frac{x}{\sqrt{x^2+y^2}} \tag{3.60}$$

$$v_{y,n}(x,y,z) = \sin\left(\pi\frac{z}{h}\right)\cos\left(n\,\mathrm{acos}\left(\frac{x}{\sqrt{x^2+y^2}}\right)\right)\frac{y}{\sqrt{x^2+y^2}} \tag{3.61}$$

$$w_{z,n}(x,y,z) = \cos\left(\pi\frac{z}{h}\right)\cos\left(n\,\mathrm{acos}\left(\frac{x}{\sqrt{x^2+y^2}}\right)\right) \tag{3.62}$$

Nonetheless, these definitions involve the trigonometric function "acos" which is not defined everywhere in the domain. Thus a decomposition of $\cos(nX)$ has been realized using Tchebytchev decomposition:

$$\cos(nX) = \sum_{k=0}^{\left[\frac{n}{2}\right]} \binom{n}{n-2k} (-1)^k \cos^{n-2k}(X)(1-\cos^2(X))^k \tag{3.63}$$

Following are some examples for the first three circumferential modes added into WAMIT:

$$U(7) = \sin\left(\pi\frac{Z}{h}\right)\left(\frac{X}{(X^2+Y^2)^{0.5}}\right)$$
$$V(7) = \sin\left(\pi\frac{Z}{h}\right)\left(\frac{Y}{(X^2+Y^2)^{0.5}}\right) \quad (3.64)$$
$$W(7) = \cos\left(\pi\frac{Z}{h}\right)$$

$$U(8) = \sin\left(\pi\frac{Z}{h}\right)\left(\frac{X}{(X^2+Y^2)^{0.5}}\right)\left(\frac{X}{(X^2+Y^2)^{0.5}}\right)$$
$$V(8) = \sin\left(\pi\frac{Z}{h}\right)\left(\frac{X}{(X^2+Y^2)^{0.5}}\right)\left(\frac{Y}{(X^2+Y^2)^{0.5}}\right) \quad (3.65)$$
$$W(8) = \cos\left(\pi\frac{Z}{h}\right)\left(\frac{X}{(X^2+Y^2)^{0.5}}\right)$$

$$U(9) = \sin\left(\pi\frac{Z}{h}\right)\left(2\,\frac{X^2}{X^2+Y^2}-1\right)\left(\frac{X}{(X^2+Y^2)^{0.5}}\right)$$
$$V(9) = \sin\left(\pi\frac{Z}{h}\right)\left(2\,\frac{X^2}{X^2+Y^2}-1\right)\left(\frac{Y}{(X^2+Y^2)^{0.5}}\right) \quad (3.66)$$
$$W(9) = \cos\left(\pi\frac{Z}{h}\right)\left(2\,\frac{X^2}{X^2+Y^2}-1\right)$$

3.2.2 Choice of material properties and natural frequency

Material properties were chosen to set the breathing mode natural frequency of the cylinder in the range of the studied wave frequencies. Table 3.1 presents material properties and geometric characteristics of the cylinder. These properties correspond to a manufactured rubber. Then mass and stiffness matrices have been calculated with

equations (3.51) and (3.52). The resulting mass and stiffness coefficients are presented in Table 3.2

Table 3.1. Material properties of the cylinder.

Parameter	Value
Radius of cylinder, R	17.5 ft
Draft of cylinder, d	200 ft
Water depth, h	200 ft
Thickness of cylinder	1 ft
Poisson's coefficient, ν	0.4
Young's modulus, E	7 MPa
Density, ρ	1500 kg/m^3

Table 3.2. Mass and stiffness coefficients.

n	Mass coefficients (kg)	Stiffness coefficients (N/m)
0	1.40E+06	7.52E+05
1	1.05E+06	1.90E+06
2	1.05E+06	7.22E+06
3	1.05E+06	1.06E+07
4	1.05E+06	1.40E+07
5	1.05E+06	1.75E+07

3.2.3 Diffraction and radiation surface elevations

Free surface elevations associated with solution of the diffraction and radiation potentials have been plotted from WAMIT output. Fig. 3.5 is the diffracted wave field and the result is similar to the one obtained with a rigid cylinder. Fig. 3.6 represents radiated wave field for the first six generalized modes. The figure indicates that the contribution of the radiated wave field to the total surface elevation becomes negligible for *n* greater than 3, especially for distances far from the cylinder.

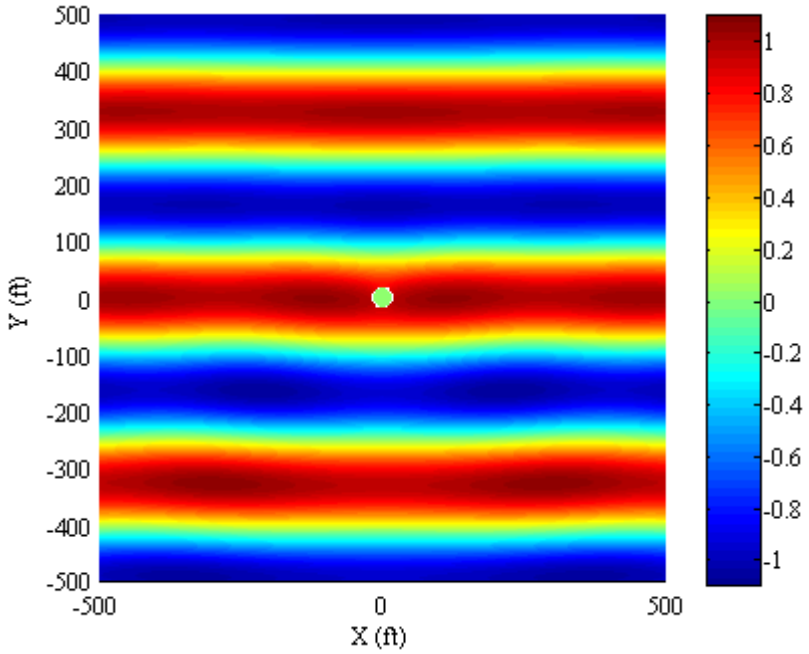

Fig. 3.5. Diffraction surface elevation from WAMIT.

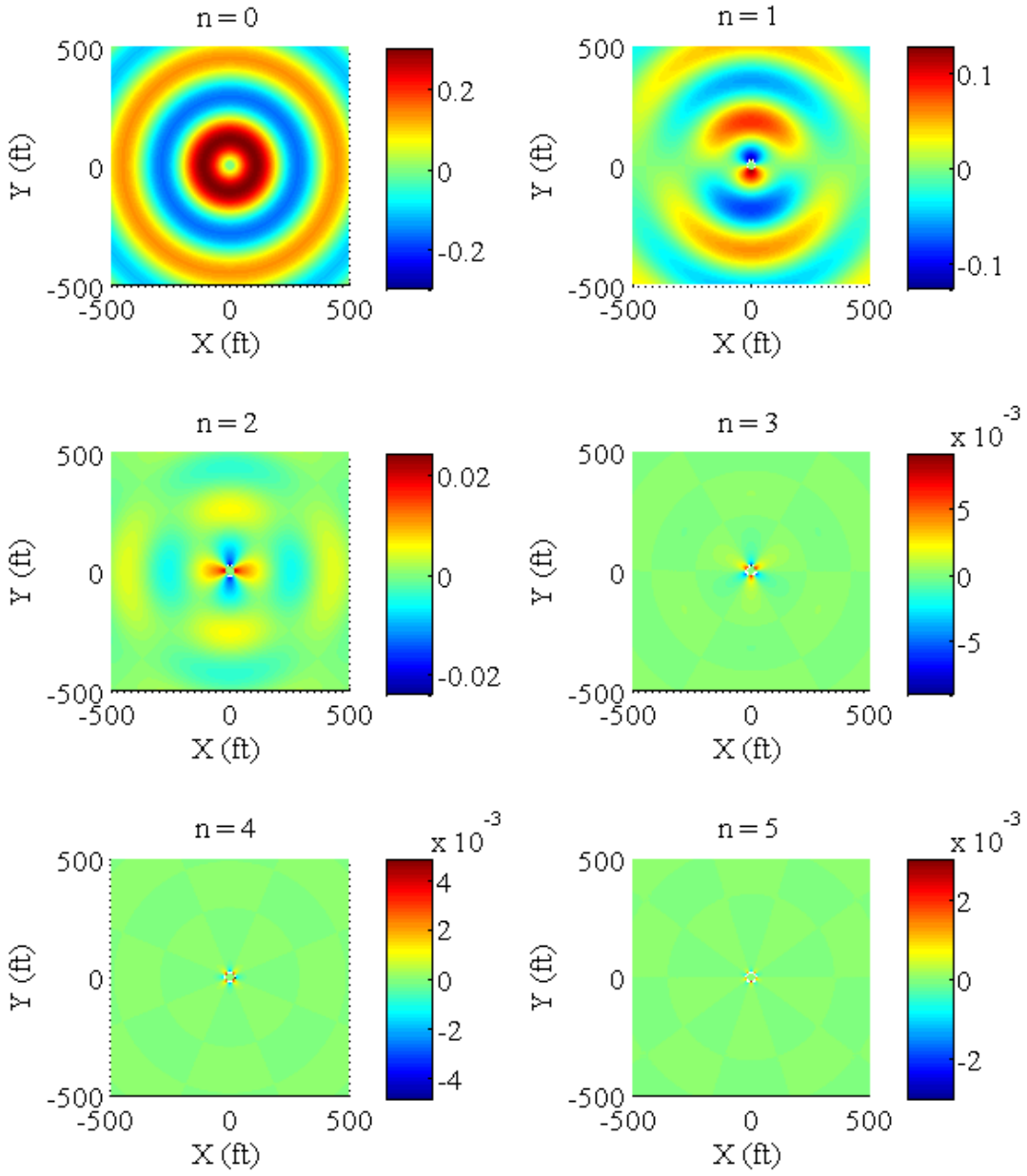

Fig. 3.6. Radiation surface elevations for the first six generalized modes.

The radiated wave field from WAMIT for the first "breathing" generalized mode is compared in Fig. 3.7 against the theoretical radiation solution formulated by Dean and Dalrymple. The third frame (c) in Fig. 3.7 indicates that the reduction in wave elevation

with radial distance is slightly larger for the WAMIT solution than it is for Dean and Dalrymple's wavemaker theory. The figure also shows that some inconsistencies exist close to the cylinder. It is possible that the formulations of the boundary conditions for a clamped-clamped shell were not correctly included in the wavemaker theory and that the evanescent part in the theoretical formulation (3.31) was not correctly computed.

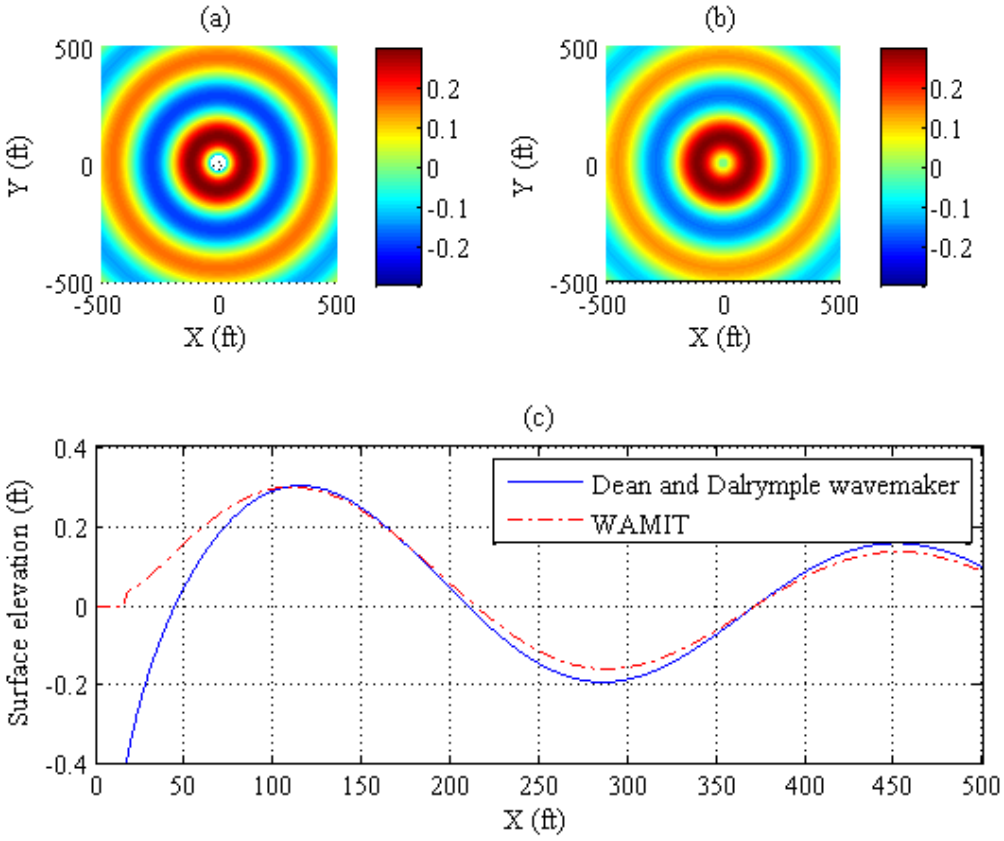

Fig. 3.7. Comparison between Dean and Dalrymple wavemaker (a) and WAMIT results for surface elevation (b) in the radial direction (c).

In addition, the Response Amplitude Operator (RAO) for the elastic cylinder is given by WAMIT and is plotted in Fig. 3.8. For the first generalized mode (n = 0), one

can observe the natural frequency of the breathing mode around 9.5 sec which is consistent with the choice of material properties discussed in the previous section.

Added-mass and damping coefficients and exciting forces calculated by both Haskind relations and direct integration of hydrodynamic pressure have also been evaluated by WAMIT and the results are shown respectively in Fig. 3.9, Fig. 3.10, Fig. 3.11 and Fig. 3.12.

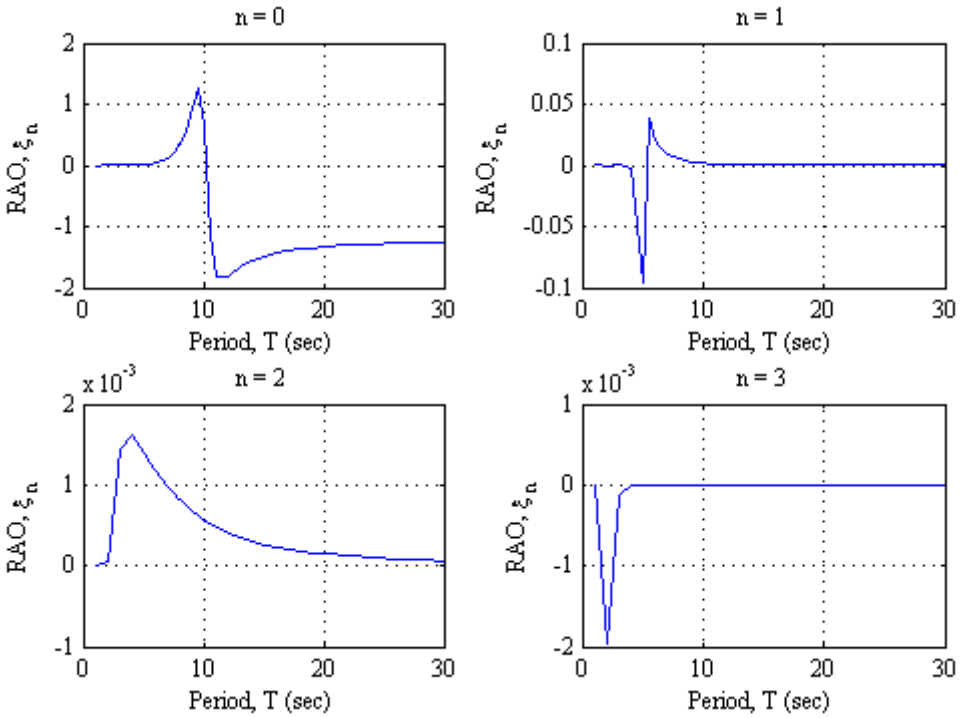

Fig. 3.8. RAO for the first four circumferential modes.

Fig. 3.8 also indicates that for higher order generalized modes, the natural period associated to the corresponding mode becomes smaller. For example, for the third mode (n = 2), the corresponding natural period is 3 sec.

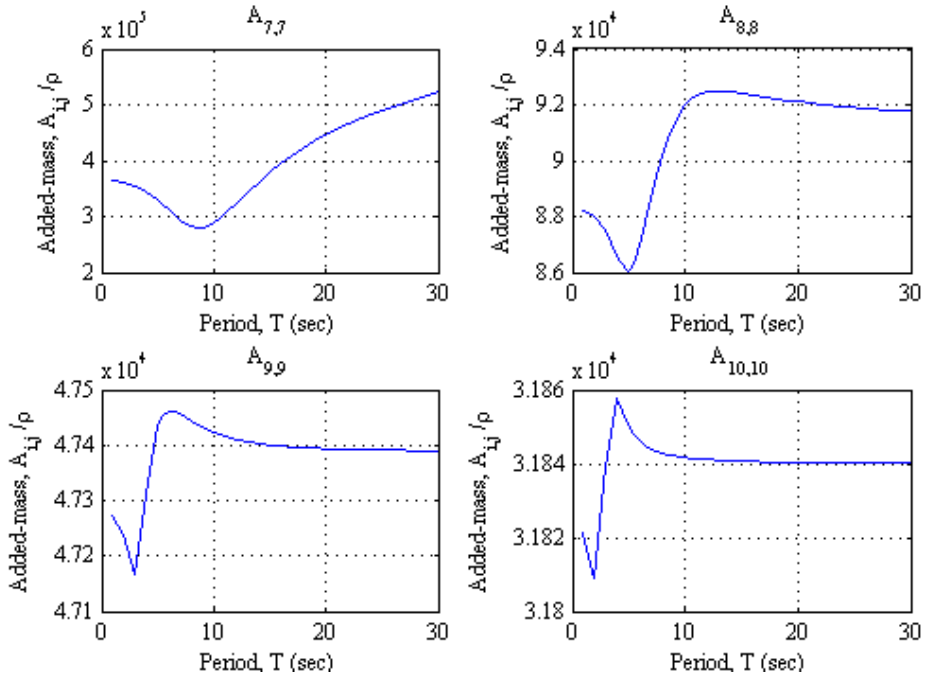

Fig. 3.9. Added-mass coefficients for the first four generalized modes.

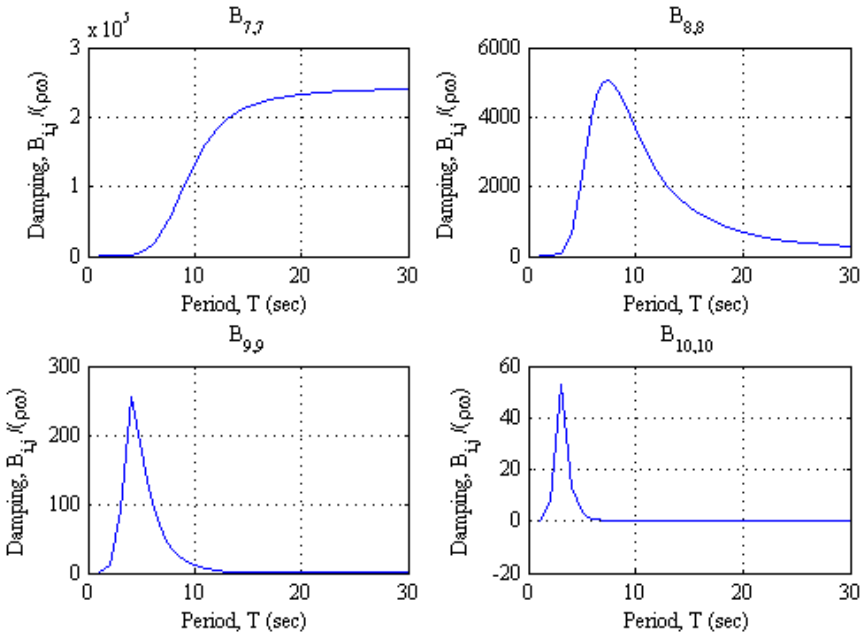

Fig. 3.10. Damping coefficients for the first four generalized modes.

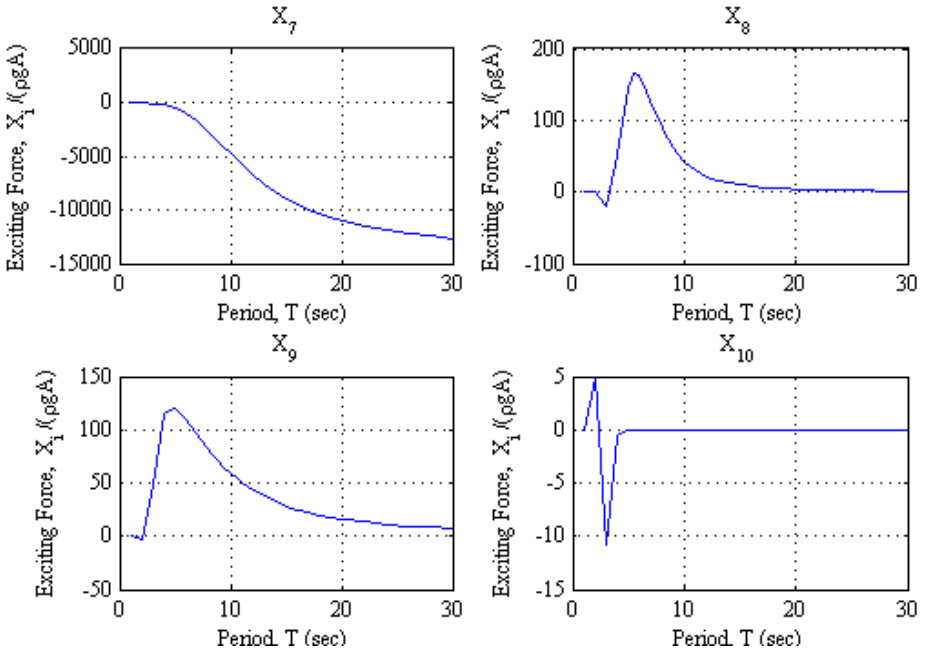

Fig. 3.11. Exciting forces from Haskind relations for the first four generalized modes.

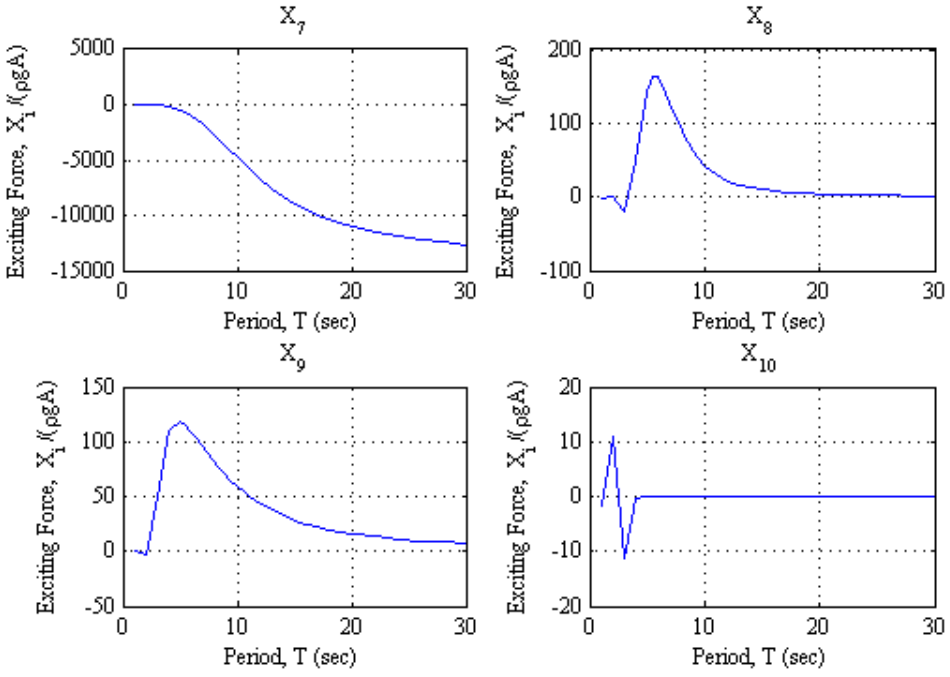

Fig. 3.12. Exciting forces from direct integration of hydrodynamic pressure for the first four generalized modes.

The exciting forces from the Haskind relations in Fig. 3.11 and the exciting forces from the direct integration of the hydrodynamic pressure in Fig. 3.12 present good agreement. The exciting forces from the Haskind relations are calculated using the radiation potentials while the exciting forces from the direct integration of the hydrodynamic pressure are evaluated using the diffraction potential. Therefore, the good agreement between both results validates our implementation of the generalized modes into WAMIT as well as the radiation solution returned by WAMIT. It also shows the accuracy for the evaluation of the velocity potentials using the high-order method in WAMIT. However, in Fig, 3.11 and Fig. 3.12, the fourth frames indicate some inconsistencies which may be resolved by increasing the resolution in azimuthal direction.

3.3 Arrays of elastic cylinders: WAMIT's results

All the preceding steps have been realized in order to study an array of elastic cylinders with WAMIT. In fact, an effective medium approach for an array of rigid cylinders have been validated by WAMIT results and circumferential deformation modes have been incorporated in WAMIT. The material properties of the cylinders inside the array may be chosen so that the natural frequency of their "breathing" mode is in the range of the studied wave periods. Therefore the interaction between long water waves and arrays of elastic cylinders may present analogous behavior as the one observed in the acoustical problem when an acoustical wave crosses a bubbly swarm.

An array of these elastic cylinders have been inputted in WAMIT. Unfortunately, our run in WAMIT did not give good results for that array, even if just the first "breathing mode" was considered. Fig. 3.13 gives an example of a random array that could be run with WAMIT. The filling ratio may be smaller than the array of rigid cylinders. In fact, the "breathing" behavior of the cylinders should accentuate wave attenuation effects.

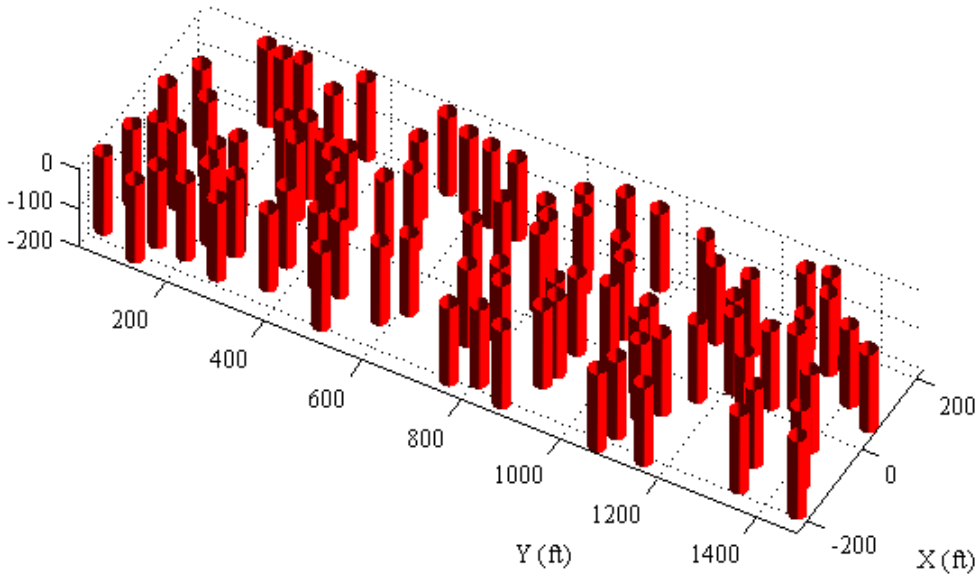

Fig. 3.13. Random array of elastic cylinders.

4. SUMMARY AND CONCLUSIONS

In this study, long wave interactions with arrays of bottom-mounted rigid and elastic vertical circular cylinders have been analyzed. The main objective was to investigate optical and acoustical analogies. The motivation behind this study was to look for wave attenuation phenomenon similar to those existing in acoustics. In fact, for certain frequencies, an acoustic wave can be attenuated while it propagates through a layer of a bubbly liquid. Wave attenuation is measured by its Insertion Loss (IL) which is frequently used in acoustics and telecommunications.

The first step was to study regular arrays of rigid cylinders in order to validate WAMIT results before studying an array of elastic cylinders. These arrays had been studied by Hu and Chan (2005) from an optical viewpoint. The effective water medium approach formulated by Hu and Chan for a semi-infinite array was used in this study and was further developed to account for the multiple reflections inside the finite-width array. Hence, the theory associated to an optical device, the Fabry-Pérot interferometer, was considered.

The other objective of this study was to use WAMIT to analyze this long wave/array interaction and develop a method to find reflection and transmission coefficients for the array. In the case of the flexible cylinders, generalized modes were incorporated to WAMIT subroutine to account for the deformation of the surface of the cylinder.

The following summaries and conclusions can be made from this study:

(a) The high-order method was used to define the geometry of the body in WAMIT. The body surface is defined by patches where the Cartesian coordinates of the points on each patch are defined by mapping functions. The advantage of this method is that for one patch, the surface is smooth with continuous coordinates and slope. The calculated velocity potential is also more accurate. In order to validate this method, the case of a single cylinder was hence studied to compare WAMIT surface elevation results to the ones predicted by MacCamy and Fuchs theory.

(b) The Maximum Likelihood Method used to determine reflection and transmission coefficients for the array was successful. These coefficients, evaluated from WAMIT surface elevation output presented good agreement with those determined by the combination of Hu and Chan's theory and the Fabry-Pérot interferometer.

(c) The specific theory associated to the effective water medium approach is applied herein in shallow water but it might be extended to deep water.

(d) For small wave periods (i.e. 7 to 10 sec), and for small wave incident angles (i.e. 0 to 30 deg), the results from WAMIT presented some inconsistencies compared to those obtained from theoretical calculations. The effective width of the array was hence discussed and an empirical formulation was stated. The effective width has to be increased for small incident angles. The empirical model linearly decreases the effective width in the heading range from 0 deg to 30 deg where it reaches the width of the

effective medium as shown in Fig. 2.18. For longer wave periods, the correction becomes less and less necessary. In fact for a wave period of 10 sec, the effective width of the array is the same as the width of the effective medium. However, this definition of the effective width should be further studied by running other cases with WAMIT.

(e) The case of a bi-convex array of cylinders was studied with WAMIT. As expected, it presents wave energy focusing properties. These results were compared with the optical theories for a converging lens. A focal length is defined and it depends on the index of the medium and the radius of curvature of the lens. Cases run with WAMIT indicated good agreements with the optical analogy. Nevertheless, the effective width of the array needs to be further studied for a complete definition of the radius of curvature.

(f) For the flexible cylinder case, generalized modes were added to WAMIT's NEWMODE subroutine. These modes are circumferential modes and they model the radial deformations of the cylinder. Because of the geometry of the system, the modes are defined in cylindrical coordinates in the literature. However, they have been transposed in Cartesian coordinates to adapt to WAMIT.

(g) From equations of motion from the theory of thin cylindrical shells, a standard set of equations of motion was derived and it allowed the definition of mass and stiffness matrices for the deformable shell.

(h) Natural frequencies associated to each mode were calculated and mass and stiffness matrices were chosen to obtain the natural period of the first "breathing mode" in the range of the studied wave periods. The Response Amplitude Operator (RAO) was plotted from WAMIT's output and indicates that the natural frequency of the "breathing" mode is actually where it was predicted from the choice of material for the cylinder (rubber).

(i) It seems that, for each generalized mode, the minimum added-mass coefficient occurs at the natural period of the mode. Nevertheless, this phenomenon has not been further studied in this thesis.

(j) Cases of arrays of elastic cylinders were run with WAMIT. Unfortunately, for the same reasons as for the random array case, the runs did not complete.

(k) The expected result for the array of flexible cylinders is an increase of the attenuation coefficient (or Insertion Loss) if the incident wave has a period in the range of the natural period of the "breathing" mode of the cylinders. The analogy with acoustical phenomenon could then be discussed. For instance, it would have been interesting to look for evidence of wave trapping and infer how much energy is transferred to evanescent modes.

Finally, recommendations can be made for future related research. By increasing the number of cases with WAMIT for the bi-convex array, the location of the focused energy point depending on the radius of curvature and refractive index could be further studied. Moreover, running random arrays of elastic cylinders with WAMIT should be more effective with a more powerful computer.

Experimental cases for arrays of both rigid and elastic cylinders would be interesting to conduct.

REFERENCES

Commander, K.W., Prosperetti, A., 1989. Linear pressure waves in bubbly liquids: comparison between theory and experiments. J. Acoust. Soc. Am 85 (2), 732-746.

Dean, R.G., Dalrymple, R.A., 1991. Water wave mechanics for engineers and scientists. Advanced Series on Ocean Engineering 2, 171-185.

Eatock Taylor, R., Huang, J.B., 1997. Second-order wave-diffraction by an axisymmetric body in monochromatic waves. Proc. R. Soc. Lond. A 453, 1515-1541.

Evans, D., Porter, R., 1997. Near-trapping of waves by circular arrays of vertical cylinders. Applied Ocean Research 19, 83–99.

Hu, X., Chan, C.T., 2005. Refraction of water waves by periodic cylinder arrays. Physical Review Letters 95, 154501, 1-4.

Junger, M.C., Cole, J.E., 1980. Bubble swarm acoustics: insertion loss of a layer on a plate. J. Acoust. Soc. Am 68 (1), 241-247.

Keller, J.B., 1964. Stochastic equations and wave propagation in random media. In: Proceedings of the Symposium in Applied Mathematics XVI, 145-170.

Kim, M. H., Yue, D. K. P., 1989. The complete second-order diffraction solution for an axisymmetric body I Monochromatic waves. J. Fluid Mech. 200, 235-264.

Leissa, A.W., 1973. Vibration of shells. Scientific and Technical Information Office NASA SP-288, 31-184.

MacCamy, R.C., Fuchs, R.A., 1954. Wave forces on piles: a diffraction theory. Tech. Memo. 69, U.S. Army Corp of Engineers, Beach Erosion Board.

McIver, P., 2002. Wave interaction with arrays of structures. Applied Ocean Research 24 (3), 121–126.

Newman, J.N., 1993. Deformable floating bodies. Eighth International Workshop on Water Waves and Floating Bodies, St. John's, Newfoundland.

Newman, J.N., 1994. Wave effects on deformable bodies. Applied Ocean Research 16, 47-59.

Siddorn, P., Eatock Taylor, R., 2008. Diffraction and independent radiation by an array of floating cylinders. Ocean Engineering 35, 1289–1303.

Sorokin, S.V., Ershova, O.A., 2005. Analysis of the energy transmission in compound cylindrical shells with and without internal heavy fluid loading by boundary integral equations and by Floquet theory. Journal of Sound and Vibration 291, 81-99.

Van Wijngaarden, L., 1968. On equations of motion for mixtures of liquid and gas bubbles. J. Fluid Mech. 33 (3), 465-474.

Walker, D.A.G., Eatock Taylor, R., 2005. Wave diffraction from linear arrays of cylinders. Ocean Engineering 32 (17–18), 2053–2078.

VITA

Name:	Aldric Baquet
Address:	Le clos Perelle, Brucourt, 14160 FRANCE
Email Address:	aldric_baquet@hotmail.com
Education:	B.S., Civil Engineering, Ecole Spéciale des Travaux Publics, 2008 M.S., Ocean Engineering, Texas A&M University, 2010